High temperature generation and equilibration of methane in terrestrial geothermal systems: Evidence from clumped isotopologues

High temperature generation and equilibration of methane in terrestrial geothermal systems: evidence from clumped isotopologues

Patrick Beaudry[a,*], Andri Stefánsson[b], Jens Fiebig[c], Jeemin H. Rhim[a,1], Shuhei Ono[a]

[a]Department of Earth, Atmospheric and Planetary Sciences, Massachusetts Institute of Technology, Cambridge, MA 02139, USA
[b]Institute of Earth Sciences, University of Iceland, Sturlugata 7, 101 Reykjavík, Iceland
[c]Institut für Geowissenschaften, Goethe-Universität, Altenhöferallee 1, 60438 Frankfurt am Main, Germany
[1]Present address: Department of Earth Sciences, Dartmouth College, Hanover, NH 03755, USA
*Corresponding author. *Email address: pbeaudry@mit.edu*

Abstract

Fluids emanating from geothermal areas contain trace quantities of methane and other simple hydrocarbons. These hydrocarbons are thought to derive from thermal cracking of organic matter dissolved in circulating meteoric or seawater or found in pre-existing organic-rich sedimentary rocks, but an abiotic origin has also been proposed. We measured the relative abundances of four CH_4 isotopologues ($^{12}CH_4$, $^{13}CH_4$, $^{12}CH_3D$, and $^{13}CH_3D$) in hydrothermal gases discharged by steam vents and geothermal wells from Iceland and Nisyros island (Greece) in order to investigate the origin of methane. Measured methane samples yielded consistently low $\Delta^{13}CH_3D$ values ($^{13}CH_3D$ abundance relative to stochastic) of 0.82 to 1.77‰, which correspond to high apparent temperatures of isotopologue equilibrium ($T_{\Delta^{13}CH_3D}$ = 278–490°C). Hydrothermal well fluids from the Krafla and Námafjall geothermal fields in Iceland yielded the lowest $\Delta^{13}CH_3D$ values, and thus the highest $\Delta^{13}CH_3D$-based temperatures averaging 438^{+55}_{-45} °C. Those samples also show the most pronounced departures in δD_{CH4} and $\delta^{13}C_{CH4}$ values expected for isotopic equilibrium with respect to δD_{H2O} and $\delta^{13}C_{CO2}$. In contrast, CH_4 samples from natural steam vents in other Iceland locations and in Nisyros have slightly higher $\Delta^{13}CH_3D$ values (with $T_{\Delta^{13}CH_3D} = 351^{+42}_{-35}$ °C) and have δD_{CH4} and $\delta^{13}C_{CH4}$ values that are consistent with those expected for isotopic equilibrium with both H_2O and CO_2. The short fluid residence times (1–50 years) in systems that are exploited for geothermal energy, such as Krafla and Námafjall, combined with the proximity of a hot magma chamber, favor the preservation of kinetic signals. The initial disequilibrium δD_{CH4} and $\delta^{13}C_{CH4}$ values are consistent with a thermogenic origin from immature organics dissolved in hydrothermally heated groundwater, but an abiotic origin cannot be excluded. The high apparent $\Delta^{13}CH_3D$-based temperatures at Krafla and Námafjall could therefore represent nonequilibrium signals associated with either pyrolysis or abiotic generation of CH_4 in a superheated vapor or supercritical water phase (>374°C), considered to exist in the roots of the system above the magmatic heat source. Isotopologue equilibration calculations demonstrate that under such conditions (e.g. >400°C) kinetic signals would be erased in days to months, implying rapid migration and quenching of CH_4 into the overlying subcritical (<300°C) hydrothermal reservoir fluids. In systems with longer fluid residence times such as Nisyros, equilibrium isotopologue distributions at temperatures of ~350°C are consistent with long fluid residence times on the order of >100 years. Our calculations further reveal that CO_2–CH_4 isotopic equilibration requires unreasonably long fluid residence times, suggesting that any apparent ^{13}C equilibrium may be coincidental.

Keywords: Methane; Isotopologues; Geothermal systems; Hydrogen isotope equilibration; Superheated vapor

1. Introduction

Most methane at the Earth's surface is ultimately derived from biological activity, either through microbial methanogenesis or by the thermal degradation of organic matter. A small fraction of Earth's CH_4 may be produced abiotically, including that formed in hydrothermal systems (Sherwood Lollar et al., 1993; McCollom and Seewald, 2006; Proskurowski et al., 2008; Klein et al., 2019; Reeves and Fiebig, 2020). Since methane is the simplest hydrocarbon (CH_4) and is often ascribed with an important role in the development of early life (e.g. Kasting et al., 2001; Ueno et al., 2006), it is of interest to characterize its various formation pathways, which can ultimately help in understanding its source on other planetary bodies (Etiope et al., 2011).

The commonly proposed pathway for abiotic production of methane involves the reduction of CO_2 by H_2, often referred to as the Sabatier reaction (e.g. Giggenbach, 1997, 1987; Klein et al., 2019; McCollom and Seewald, 2006) :

$$\mathrm{CO_2 + 4H_2 \rightleftharpoons CH_4 + 2H_2O} \qquad (1)$$

For example, high concentrations of CH_4 found in many serpentinization environments have been attributed to this reaction, where the reducing conditions (high fH_2) imposed by serpentinization reactions provide a thermodynamic drive for CH_4 formation, with mantle CO_2 or dissolved carbonate of seawater or meteoric water origin as the source of inorganic carbon (Shock, 1992; Klein et al., 2019). Hydrolysis-induced oxidation of ferrous iron drives the evolution of serpentinization systems towards high fH_2 after prolonged water-rock interaction, and is favored in host rocks with high Fe (II) contents and increasing fluid pH (Leong and Shock, 2020).

Geothermal systems are also characterized by dynamic multiphase reactions and metastable equilibria with evolving fluid pH and precipitation of secondary minerals, which have important controls on redox conditions and fH_2 (Giggenbach, 1987; Arnórsson et al., 2007; Stefánsson, 2017). However, the generally lower Fe (II) content of rocks in geothermal vs. serpentinization systems is less favorable for H_2 generation and thus CH_4 production. Furthermore, the reduction of CO_2 to CH_4 and other hydrocarbons has a high activation energy and is shown to be sluggish under single-liquid phase hydrothermal conditions (McCollom, 2016; Seewald et al., 2006). Nevertheless, based on bulk stable isotope compositions of geothermal CH_4, in particular on elevated $\delta^{13}C$ values compared to conventional thermogenic sources, it has been proposed that methane found in geothermal environments is of abiotic origin (Fiebig et al., 2007; Etiope and Sherwood Lollar, 2013). However, observed $\delta^{13}C_{CH4}$ and δD_{CH4} patterns also follow trends of thermogenic CH_4 formation, such that most (if not all) geothermal methane could derive from the pyrolysis of organic matter brought to depth by circulation of surface derived waters (Des Marais et al., 1981; Fiebig et al., 2019).

This poses the question as to what conditions are most favorable for abiotic methane production. On the one hand, reaction (1) is exothermic, with a ΔH of reaction ranging from -250

to -210 kJ/mol between 100°C and 500°C (based on SUPCRT92; Johnson et al., 1992), such that production of methane is favored at lower (<300°C) temperatures but kinetics become increasingly sluggish. On the other hand, higher temperatures promote faster rates of reaction (and hence of CH_4 production), albeit with less thermodynamic drive. In addition to the temperature control, experimental studies suggest that the presence of a vapor phase, as opposed to an entirely aqueous phase, promotes methane production from CO_2 reduction (McCollom, 2016, 2013 and references therein). The faster rate of CO_2 reduction in a gas phase supports the hypothesis that methane in seafloor hydrothermal vents could have been generated abiotically in fluid inclusions within the oceanic lithosphere, and later extracted by circulating hydrothermal fluids (Kelley, 1996; McDermott et al., 2015; Wang et al., 2018; Klein et al., 2019; Labidi et al., 2020). In geothermal systems, the combination of high temperatures with processes that promote the formation of a vapor phase could overcome the kinetic inhibitions associated with abiotic methane.

Chemical and isotope geothermometers can give valuable insight into the thermal evolution of solutes, gases and isotopes in hydrothermal fluids. Chemical geothermometers are based on the fundamental assumption of chemical equilibrium between various gaseous and aqueous species and/or hydrothermal minerals at a particular temperature (e.g., Arnórsson et al., 1983a; Chiodini and Marini, 1998; D'Amore and Panichi, 1980; Giggenbach, 1988; Gunnarsson and Arnórsson, 2000). Isotope thermometers, which rely on the isotopic fractionation between gaseous and/or aqueous species, can preserve more intricate signals of subsurface temperatures and processes, although they can also be affected by kinetic effects (Richet et al., 1977; Giggenbach, 1982; Ohmoto and Lasaga, 1982; Horibe and Craig, 1995; Giggenbach, 1997; Horita, 2001; Fiebig et al., 2004). Other processes may control or affect these apparent equilibria, for example sources of elements (and thus initial isotopic compositions), sluggish reaction kinetics, and secondary processes in the fluid conduit from reservoir to surface like boiling and mineral formation (Arnórsson et al., 2007). Substantial discrepancies are commonly obtained between temperatures calculated from different geothermometers. This may reflect either different closure temperatures of a particular chemical or isotope reaction, different initial degrees of disequilibrium controlled by reaction kinetics, and/or different responses to secondary processes and re-equilibration (Giggenbach, 1987; Chiodini and Marini, 1998; Arnórsson et al., 2007; Stefánsson, 2017).

Geothermometers based on the relative concentrations and ^{13}C fractionation between CH_4 and CO_2 converge to similar temperatures (often ~300-350°C) for several geothermal areas, including those found in Yellowstone, New Zealand and Nisyros (Craig, 1953; Hulston and McCabe, 1962; Giggenbach, 1982; Giggenbach, 1997; Fiebig et al., 2004), which has led to the suggestion that abiotic CH_4 is produced through reaction (1). However, since the δD and $\delta^{13}C$ systematics of hydrothermal CH_4 and higher n-alkanes in several locations can also be explained by open-system thermal cracking of marine or terrestrial organic matter (Fiebig et al., 2019), observed equilibrium ^{13}C fractionations in some systems might be fortuitous. This is explained by the maturation trend of organic matter, where thermal cracking of mature organic matter produces CH_4 with higher $\delta^{13}C$, in apparent isotopic equilibrium with mantle CO_2. Moreover, evidence for the natural occurrence of reaction (1) in geothermal systems, in particular with regards to the existence of an efficient catalyst under hydrous conditions, is still lacking. It follows that chemical equilibrium between CO_2-CH_4-H_2 may not be attained as often as has been

previously suggested (e.g. Giggenbach, 1997), owing to the complex reaction pathways and intermediates involved in the abiotic reduction of CO_2 (Seewald et al., 2006) , written in its simplified version as reaction (1).

Measurements of the relative abundances of methane isotopologues ($^{12}CH_4$, $^{13}CH_4$, $^{12}CH_3D$, $^{13}CH_3D$ and $^{12}CH_2D_2$) can be used to calculate the temperatures that correspond to internal isotopologue equilibria (Ono et al., 2014; Stolper et al., 2014a; Wang et al., 2015; Stolper et al., 2017; Young et al., 2017). The metrics $\Delta^{13}CH_3D$ and $\Delta^{12}CH_2D_2$ represent the excess abundance of each doubly-substituted isotopologue ($^{13}CH_3D$ and $^{12}CH_2D_2$, respectively) relative to a stochastic distribution, and become smaller with increasing temperature. These clumped isotopologue fractionations can be compared to isotopic fractionations between CH_3D vs. HDO and $^{13}CH_4$ vs. $^{13}CO_2$ to examine the degree of equilibrium or disequilibrium among these three independent isotope/isotopologue systems (Wang et al., 2018; Labidi et al., 2020). Previous applications of the clumped CH_4 isotopologue geothermometer reported apparent $\Delta^{13}CH_3D$-based temperatures in marine hydrothermal vents ranging from 160°C to 360°C (Wang et al., 2018; Labidi et al., 2020). Compared to seafloor vents, methane from terrestrial fumaroles measured to date shows higher apparent equilibrium temperatures, ranging from 350 to 580°C (Douglas et al., 2017). We note that the measurements of Douglas et al. (2017) were reported as Δ_{18} values, which differ slightly from $\Delta^{13}CH_3D$ since it incorporates both methane isotopologues of mass 18 ($^{13}CH_3D$ and $^{12}CH_2D_2$). Accurate conversion between Δ_{18} and $\Delta^{13}CH_3D$ values requires the measurement of $^{12}CH_2D_2$. Since $^{13}CH_3D$ is approximately 50 times more abundant than $^{12}CH_2D_2$, however, the value of Δ_{18} is expected to be close to $\Delta^{13}CH_3D$ for natural methane samples. The use of these different proxies depends on the analytical procedure, since in early clumped CH_4 studies by mass spectrometry $^{13}CH_3D$ and $^{12}CH_2D_2$ peaks were not well resolved (Stolper et al., 2014b). Spectroscopic measurements (as those performed here) are not affected by this overlap. The relatively low Δ_{18} values measured for CH_4 from terrestrial fumaroles are of interest because their corresponding high apparent temperatures often exceed the critical temperature of pure water (T_c = 374°C), which would imply generation or equilibration of CH_4 in a supercritical water or superheated vapor phase (above critical temperature but below critical pressure of water; Fig. 1). Such fluids have been suggested to exist at the contact between hydrothermal systems and magmatic heat sources (Hayba and Ingebritsen, 1997; Scott et al., 2015; Heřmanská et al., 2019). Alternatively, low $\Delta^{13}CH_3D$ values could also be explained by kinetic effects during thermal cracking of organic matter (e.g. Shuai et al., 2018a), highlighting gaps in our understanding of the origins of geothermal CH_4.

In this study, we measured the relative abundances of CH_4 isotopologues ($^{12}CH_4$, $^{13}CH_4$, $^{12}CH_3D$, and $^{13}CH_3D$) in steam vents and hydrothermal well fluids from Iceland and Nisyros island (Greece) in order to constrain the origin of methane in terrestrial geothermal settings. In addition, measurements of $^{12}CH_2D_2$ from two Nisyros samples were reported in Gonzalez et al. (2019). Our sample set covers a wide range of geothermal environments, characterized by a variable range of hydrothermal fluid reservoir temperatures, variable fluid residence times and ascent durations to surface. Some of the systems studied, for example Krafla, have also been observed to contain a high-temperature supercritical or superheated fluid reservoir (>400°C) below the conventional subcritical reservoir (~200-300°C). Our results imply that isotope and isotopologue equilibrium might be achieved for CH_4 in long-lived natural geothermal settings, but

significant disequilibria are observed for samples from higher-permeability systems where fluid circulation is accelerated by the operation of active geothermal wells. We discuss the relative rates of isotope/isotopologue exchange to relate isotopologue equilibration with fluid residence times. The measured disequilibrium signals can be explained by a thermogenic origin for methane, but our data does not rule out the possibility of abiotic synthesis.

2. Geological context and sample description

2.1 Iceland

Iceland is located at the intersection of a hotspot and the mid-Atlantic ridge, giving rise to unusually high heat flow and crustal production rates (Gudmundsson, 2000), reflected by the existence of several active volcanoes. The island is host to over thirty high-temperature geothermal systems (e.g. Ármannsson, 2016), which are located along the active volcanic belts running in a SW-NE trend across the country (Fig. 2A). The development of these systems is thought to be related to the emplacement of intrusive bodies and formation of sub-vertical dykes and fractures leading to high permeability (Arnórsson, 1995), which promotes heating of groundwaters. Decades of geothermal exploration and development have generated a wealth of chemical and isotopic data on Icelandic hydrothermal fluids (Arnórsson et al., 1983a; Ármannsson et al., 1987; Gudmundsson, 2000; Stefánsson et al., 2017; Stefánsson, 2017), and geothermal wells have helped characterize basement geology and alteration assemblages (Ármannsson et al., 1987; Pope et al., 2016). The source water is in most places identified as shallow groundwater of meteoric origin (Stefánsson, 2017), although the hydrothermal systems along the Reykjanes peninsula are dominated by seawater. Surface manifestations in high-temperature areas are usually steam vents (fumaroles), mudpots and highly altered ground. Wells sunk in geothermal fields have typical depths of ~1.5-3 km and reservoir temperatures between 200 and 300°C (Arnórsson, 1995; Ármannsson, 2016). Higher temperature reservoirs with supercritical/superheated reservoir temperatures have also been observed through the drilling activity of the Iceland Deep Drilling Project, for example at Krafla where drilling into magma (IDDP-1) at a depth of 2 km resulted in 440°C fluids (Elders et al., 2014) and at Reykjanes where the bottom-hole temperature of a ~4.5 km borehole (IDDP-2) was ~600°C (Bali et al., 2020).

We collected fluid samples from steam vents (vapor) and geothermal wells (vapor + liquid) spanning the active volcanic zone in Iceland, from the Reykjanes geothermal well field in the SW, Kerlingarfjöll area in the central highlands, to the Krafla and Námafjall geothermal fields in the NE (Fig. 2A). The source of H_2O in most samples is meteoric, based on its isotopic composition (δD and δ^{18}O) generally corresponding to local precipitation (Stefánsson et al., 2017), except for one well sample from Reykjanes where the δ^{18}O and δD values of the liquid water correspond closely with those of seawater (Stefánsson et al., 2017).

2.2 Nisyros, Greece

Nisyros (Fig. 2B) is the easternmost island of the Aegean volcanic island arc, and is located about 15 km west of the Turkish coast. With a total diameter of ~8 km, it is host to a 4-km-wide, 250-m-deep central caldera which contains several hydrothermal explosion craters with many

active fumaroles (Di Paola, 1974). The most recent of these craters were formed in a series of hydrothermal eruptions historically recorded in the years 1871, 1873 and 1887, during which large rock fragments were ejected and important quantities of steam discharged (Marini et al., 1993 and references therein). Two geothermal wells were drilled in the early 1980's, up to depths of 1816 and 1547 m, and indicated reservoir temperatures above 300°C (Chiodini et al., 1993). These wells identified the presence of carbonate basement and of shallow and deep permeable zones, with potassic-propylitic mineral assemblages at the bottom of the deepest well suggesting temperatures above 350°C (Marini et al., 1993). High reservoir temperatures were also reflected by the presence of high-enthalpy fluids in this deep permeable zone (Chiodini et al., 1993; Marini et al., 1993). It is thought that the deep aquifer was involved in the 1873 eruption, evidenced by the high Cl content of the discharged brine (Marini et al., 1993). The seawater-dominated geothermal system at Nisyros and the geochemistry of steam emanations have been well characterized (Kavouridis et al., 1999; Brombach et al., 2003; Fiebig et al., 2004; Fiebig et al., 2013). We sampled gas-rich steam from 9 fumaroles spanning four distinct phreatic craters within the central caldera (Fig. 2B). Previous investigations have suggested that CH_4 and CO_2 occur in chemical and isotopic equilibrium at a temperature of ~350°C (Fiebig et al., 2004; Fiebig et al., 2013), but the concentrations and $\delta^{13}C$ signatures of higher hydrocarbons point to a thermogenic origin, suggesting that observed chemical and isotopic equilibrium may be coincidental (Fiebig et al., 2019).

3. Methods

Samples were collected in Iceland in August 2015 and in Nisyros in October 2017. For well samples, the liquid and vapor phases were separated using a Webre separator prior to sampling (Arnórsson et al., 2016). Samples of fumarole vapor were collected by inserting a titanium rod into the vapor outlet. Geothermal vapor was subsequently collected into various gas bottles.

For major gas determination, 125 ml evacuated glass flasks partially filled with ~10-50 ml 50% KOH (Iceland) or 4M NaOH (Nisyros) were used. The non-condensable gases including H_2, N_2, CH_4 and Ar were analyzed using a gas chromatography (GC) system equipped with a thermal conductivity detector (TCD) whereas the condensable gases including H_2S and CO_2 were analyzed in the vapor condensate using Hg-precipitation and modified alkalinity titrations, respectively (Arnórsson et al., 2006; Stefánsson et al., 2007). Separate dry-gas samples were collected for CO followed by GC analysis using a pulsed discharge detector (PDD) (Table 1).

Samples for δD_{H2O} measurements were collected into gas-tight glass bottles after condensation in line using a glass cooling spiral (Cioni and Corazza, 1981). For δD_{H2O} analysis, the hydrogen was extracted by the H_2-water equilibration method using a Pt-catalyst (Horita, 1988) followed by analysis using a Finnegan MAT 251 ion ratio mass spectrometer (IRMS) at the University of Iceland and the results reported in terms of the conventional δ-notation in ‰, relative to the VSMOW standard. Replicate analysis of the reference material yielded a standard deviation of 0.7‰.

Dry gas samples were collected for carbon isotope analysis of CO_2 ($\delta^{13}C_{CO2}$), which was performed at Goethe University, using a Flash EA 1112 (ThermoFisher) connected to a MAT 253 gas source mass spectrometer (Fiebig et al., 2004). CO_2 from two bottles (Oztech), each calibrated

against VPDB, was measured along with the samples to correct for potential instrumental fractionations and scale compression. Hydrocarbon distribution ratios (C_1/C_{2+}) were also determined at Goethe University as outlined by Fiebig et al. (2015).

Samples for methane clumped isotopologue determination were collected into 1L pre-evacuated glass bottles containing ~200 mL 50% KOH (Iceland) or 4M NaOH (Nisyros). Methane was extracted and purified from the gas phase of the flask samples by repeated cycles of vacuuming and flushing with a He carrier gas through a cold trap filled with activated charcoal submerged in liquid nitrogen (-196°C), as described by Wang et al. (2015). This traps gases such as CH_4, N_2, CO, and traces of CO_2 that remained in the gas phase. The trap was then heated to separate adsorbed gases through a gas chromatography column packed with Carboxen-1000 (MilliporeSigma, St Louis, MI) held at 30°C, and eluted methane was trapped again in a U-trap containing silica gel at liquid nitrogen temperature. The purified CH_4 samples ranged in volume from 0.7 to 10 ml (STP). The relative abundances of methane isotopologues $^{12}CH_4$, $^{13}CH_4$, $^{12}CH_3D$ and $^{13}CH_3D$ were measured by a tunable infrared laser direct absorption spectroscopy (TILDAS) instrument as described previously (Ono et al., 2014; Wang et al., 2015). Two samples from Nisyros were measured for $^{12}CH_2D_2$ (in addition to the four isotopologues mentioned above) by another TILDAS instrument and reported in Gonzalez et al. (2019).

Sample measurements were bracketed by measurements of CH_4 standard gases of known isotopic composition (δD and $\delta^{13}C$) spanning a large δD range (~200 ‰), which were heated to 250°C for at least two weeks with a Pt catalyst to ensure isotopologue equilibrium (Ono et al., 2014). Isotope values are reported using standard delta notation against VPDB and VSMOW for the ratios $^{13}C/^{12}C$ and D/H, respectively. This isotope scale was calibrated by the measurements of NGS-1 and NGS-3 (Wang et al., 2015). We used the reference $\delta^{13}C$ values of -29.0 and -72.8‰, and δD of -138 and -176‰, for NGS-1 and NGS-3, respectively (Hut, 1987).

Results in Table 2 show the 95% confidence interval for the spectroscopic measurements, typically 0.2 to 0.4‰ for $\Delta^{13}CH_3D$ values. This does not include potential fractionation during sample preparation. One sample from Iceland (15-AS-03) was collected twice and analyzed as duplicates (Table 2), showing good reproducibility between duplicates with compounded errors similar to the 95% confidence intervals of the measurements (Table 2). Most samples (samples with less than 5ml CH_4) were measured in a recycling mode, in which sample CH_4 is recovered from the TILDAS absorption cell to the cold trap, and reintroduced to TILDAS for 6 to 10 times. This allows repeated comparison of sample against reference gas. Thus, precision is not necessarily a function of sample size.

We define $\Delta^{13}CH_3D$ as a measure of the abundance of $^{13}CH_3D$ relative to a stochastic distribution (Ono et al., 2014):

$$\Delta^{13}\mathrm{CH_3D} = \ln\left(\frac{^{13}\mathrm{CH_3D}}{^{12}\mathrm{CH_3D}} \cdot \frac{^{12}\mathrm{CH_4}}{^{13}\mathrm{CH_4}}\right) \quad (2)$$

The relationship between $\Delta^{13}CH_3D$ values and apparent methane generation temperatures used in this study is based on the formula:

$$\Delta^{13}\mathrm{CH_3D(T)} = -0.11006\left(\frac{1000}{T}\right)^3 + 1.04151\left(\frac{1000}{T}\right)^2 - 0.55235\left(\frac{1000}{T}\right) \quad (3)$$

This equation is approximated from the solution based on the fundamental vibrational frequencies as described in Whitehill et al. (2017).

We note here that different theories predict a different temperature dependence for the value of $\Delta^{13}CH_3D$ (e.g. Eldridge et al., 2019; Liu and Liu, 2016; Wang et al., 2015; Webb and Miller, 2014). This will affect our results in two ways: one directly affects the reported $\Delta^{13}CH_3D$ values and the other affects the equilibrium temperatures derived from given $\Delta^{13}CH_3D$ values. In this study, we used methane equilibrated at 250°C to anchor the $\Delta^{13}CH_3D$ value of our reference gas. We define this value as 1.98‰ **Error! Reference source not found.**, which is 0.09‰ lower than the value of 2.07‰ obtained using the recent calibration by Eldridge et al. (2019). Our unknown sample measurements are calibrated against this 250°C heated methane, therefore in general $\Delta^{13}CH_3D$ values reported in this study (Table 2) are <0.1‰ lower than they would be using the equation of Eldridge et al. (2019). Apparent equilibrium temperatures are in turn calculated from these $\Delta^{13}CH_3D$ values using **Error! Reference source not found.**. Due to the relative consistency of the temperature dependence of $\Delta^{13}CH_3D$ applied both to our equilibrium reference CH_4 at 250°C and to the observed range of $\Delta^{13}CH_3D$ values, the derived equilibrium temperatures do not differ significantly between different theories. For example, we would report a temperature of 350°C for a $\Delta^{13}CH_3D$ measurement of 1.34‰. The same measurement may yield e.g. 1.43‰ if the calibration of Eldridge et al. (2019) is used to anchor our reference gas, which would return a temperature of 346°C. Such a difference is considerably smaller than the 95% confidence intervals reported in Table 2, hence the application of different models is not expected to significantly alter our results.

4. Results

The chemical composition of Iceland and Nisyros steam samples are shown in Table 1. Isotopic compositions of H_2O (δD), CO_2 ($\delta^{13}C$) and CH_4 ($\delta^{13}C$ and δD), including clumped isotopologue signatures ($\Delta^{13}CH_3D$), are reported in Table 2. All samples have $\delta^{13}C_{CH4}$ and δD_{CH4} values that plot in a field originally proposed as 'abiotic' (Etiope and Sherwood-Lollar, 2013) but also defined as 'volcanic thermogenic' (Reeves and Fiebig, 2020) (Fig. 3, Table 2).

Iceland samples display a large isotopic variability, with δD_{CH4} ranging from -319.6‰ to -165.0‰ and $\delta^{13}C_{CH4}$ ranging from -39.6‰ to -25.0‰. While some of the δD variability can be attributed to the source of water in the hydrothermal system (meteoric vs seawater), pronounced $\delta^{13}C$ and δD heterogeneities are observed at the local scale, especially in the Krafla and Námafjall geothermal areas. In contrast, all Nisyros samples yield homogeneous δD_{CH4} and $\delta^{13}C_{CH4}$ values, with δD_{CH4} ranging from -124.4‰ to -135.4‰ and $\delta^{13}C_{CH4}$ from -21.8‰ to -23.4‰. The majority of samples have $\Delta^{13}CH_3D$ values ranging from 0.82‰ to 1.77‰, corresponding to an apparent equilibrium temperature range from 278^{+56}_{-44} to 490^{+163}_{-99} °C, aligned with previous measurements of CH_4 isotopologues in geothermal systems (Fig. 4).

Additionally, measurements of $\Delta^{13}CH_3D$ and $\Delta^{12}CH_2D_2$ of two Nisyros samples (samples K7 and S4-hi) were made on a separate TILDAS instrument and reported by Gonzalez et al. (2019). The reported $\Delta^{13}CH_3D$ values of 0.97 ± 0.10‰ and 1.14 ± 0.30‰, corresponding to apparent temperatures of 447^{+26}_{-23} and 400^{+90}_{-65}°C, agree within uncertainty with the values reported in this

study of 1.16 ± 0.21‰ and 1.37 ± 0.30‰ (390^{+56}_{-45} and 345^{+69}_{-52}°C, respectively). Low $\Delta^{12}CH_2D_2$ values of 0.2 ± 0.4‰ and -0.01 ± 0.6‰ give apparent equilibrium temperatures of 860^{+122}_{-91} and >769°C.

5. Discussion

5.1. Equilibrium and disequilibrium signals for chemical and isotopologue geothermometers

In order to interpret apparent temperatures derived from the methane isotopologue geothermometer, we compare them with several other chemical and isotope geothermometers, and with reservoir temperatures measured directly downhole, which are available for well samples. We first evaluate geothermometers commonly used for geothermal exploration, such as quartz solute equilibria (Gunnarsson and Arnórsson, 2000) and various gas geothermometers (Arnórsson and Gunnlaugsson, 1985; Arnórsson et al., 1998). We then explore geothermometers that involve methane isotopologues, which include those based on deuterium fractionation between H_2O–CH_4 ($\alpha_{H2O-CH4}$), ^{13}C fractionation between CO_2–CH_4 ($\alpha_{CO2-CH4}$), and internal equilibrium characterized by the relative abundances of CH_4 isotopologues ($\Delta^{13}CH_3D$). These solute, gas and isotope geothermometers are tabulated in Table 3.

5.1.1. Measured, solute and gas geothermometry temperatures

Solute geothermometers are often applied to determine hydrothermal reservoir temperatures (Arnórsson et al., 1983b; Giggenbach, 1988; Gunnarsson and Arnórsson, 2000). The solubility of quartz (Table 3) is a widely applied geothermometer, which generally agrees with measured downhole temperatures (Table 4 and Fig. 5A). Hence, geothermal wells provide the advantage of sampling fluid directly from the hydrothermal reservoir where the temperatures are known with a reasonable degree of confidence, to which other geothermometers can be compared in order to gain insight on the evolution of the hydrothermal systems.

The majority of our samples, however, come from fumaroles, where measured or quartz temperatures are unavailable. Therefore, we must turn to gas compositions (Table 1) to estimate reservoir temperatures. The use of gas geothermometry relies on the concentrations of gas species within a separated vapor phase, which depends on the extent of fluid-rock interactions in the geothermal system and saturation of the fluid with various secondary minerals (e.g. calcite, epidote, pyrite), as well as on the vapor/liquid partition coefficients of the various gas species. Such geothermometers can be estimated by considering theoretical equilibria of various reactions (e.g. Chiodini and Marini, 1998; Giggenbach, 1980), or constructed empirically by calibrating measured concentrations with measured reservoir temperatures, e.g. from geothermal wells (e.g. Arnórsson et al., 1998; Arnórsson and Gunnlaugsson, 1985; D'Amore and Panichi, 1980). Here we combine three different gas geothermometers based on concentrations of CO_2, H_2S, and CO_2/N_2 ratios (Table 3), which were empirically calibrated by Arnórsson and Gunnlaugsson (1985) and updated by Arnórsson et al. (1998). Figure 5B shows the comparison of gas temperatures to the measured reservoir temperatures for well samples. While the agreement is not as striking as that for quartz geothermometry (Fig. 5A), the temperatures are

generally within 50°C of each other. We also note that the two samples that are furthest from the measured temperatures, Krafla-16 and Námafjall-13, have excess enthalpy (see Table 4), thus the vapor phase composition is more likely to have been modified by boiling or phase segregation, which could have important effects on calculated gas temperatures (e.g. Arnórsson et al., 2007; Chiodini and Marini, 1998). This issue should be less critical for fumaroles, which emit steam at ~100°C and atmospheric pressure. Therefore, gas temperatures calculated for fumarole samples are taken to represent relatively well the temperatures of boiling in the hydrothermal reservoir at depth.

In general, Iceland samples have reservoir temperatures between 250°C and 300°C, which are systematically lower than $\Delta^{13}CH_3D$-based temperatures (Fig. 5C, Table 4). This effect is most pronounced for Krafla and Námafjall wells, while the fumarole sample from Krysuvík shows closest agreement between $\Delta^{13}CH_3D$ and reservoir temperature. In contrast, gas concentrations from Nisyros samples point to reservoir temperatures around 350°C, which is in good agreement with previously-determined temperatures obtained with other independent geothermometers (Brombach et al., 2003) or based on metamorphic assemblages (Marini et al., 1993). Importantly, these are also in agreement with $\Delta^{13}CH_3D$-based temperatures (average ±1 s.d.) of 355^{+50}_{-41} °C.

We also compare the temperatures and depths of two-phase well fluids to the pressure-temperature curve of boiling water (Fig. 6). Discharge temperatures and pressures measured at the well head reflect the cooling of ascending fluids through adiabatic boiling and thus usually fall on the boiling point curve. In contrast, temperatures measured at depth for the different wells are lower than those expected for boiling at hydrostatic pressure, reflecting the depressurization of fluids when they are intersected by geothermal wells (e.g. Arnórsson et al., 2007).

5.1.2. Deuterium fractionation between H_2O and CH_4

While comparison between measured reservoir temperatures, solute and gas geothermometry indicates close to mineral-fluid equilibration at subcritical temperatures (Fig. 5A, B), hydrogen isotope fractionation between H_2O and CH_4 ($\alpha_{H2O–CH4}$) indicates different degrees of disequilibrium and equilibrium (Fig. 7A, B). The variability is considered to reflect the sluggish kinetics of isotopic exchange between H_2O and CH_4 (Table 3) due to the chemical stability of methane C-H bonds. Samples exhibit two linear trends of increasing δD_{CH4} values with δD_{H2O} around -90‰ and -10‰ (Fig. 7A), reflecting Icelandic meteoric water and seawater sources, respectively, where maximum δD_{CH4} values associated with each trend are indicative of isotopic equilibrium with the source water in the hydrothermal reservoirs. For example, local seawater is associated with higher δD_{CH4} for Nisyros and Reykjanes and low δD meteoric water is associated with lower δD_{CH4} for other Icelandic sites. Alternatively, the source water could exchange hydrogen isotopes with dissolved or particulate organic matter prior to thermogenic cracking, which would also cause subsequently generated CH_4 to have δD signatures partly derived from local H_2O.

Steam vents in Nisyros island yielded relatively homogeneous δD_{CH4} values: CH_4 from three sites, Kaminakia, Stefanos and Polybotes Mikros, yielded an average δD_{CH4} of -125.5 ± 1.1‰ (± 1 s.d.), whereas Phlegeton yielded -135.4‰ (Table 2). There is a large variability in δD_{H2O}

values, but this is mostly due to three outliers, with K7 having a very depleted δD_{H2O} value of -56.5‰, and the two vents from Alexandros having δD_{H2O} of -4.5‰ and -4.8‰. The depletion observed for K7 is likely due to removal of heavy water through partial condensation occurring during the upflow of steam, which is more likely to occur at the lower vent temperatures measured at Kaminakia (Table 4) (Brombach et al., 2003; Fiebig et al., 2004). The other samples have similar δD_{H2O} values with an average (±1 s.d.) of -11.0 ± 1.6‰, which is indistinguishable from the parental hydrothermal liquid, previously suggested to be a mixture between seawater and "andesitic" water with δD_{H2O} of -11 ± 5‰ (Brombach et al., 2003; Fiebig et al., 2004). Therefore, overall $\alpha_{CH4\text{-}H2O}$ values at Nisyros reflect apparent isotopic equilibrium around 300–350°C (Fig. 7A, B), consistent with gas geothermometry and previous determinations of the hydrothermal reservoir temperature (Brombach et al., 2003; Fiebig et al., 2004; Fiebig et al., 2013).

Methane from Kerlingarfjöll steam vents in Iceland also has δD_{CH4} values that can be interpreted as being in D-equilibrium with H_2O at reservoir temperatures of ~250–300°C, if we infer values for δD_{H2O} between -80 and -90‰, corresponding to local precipitation (e.g. Stefánsson et al., 2017b) (Table 2 and Fig. 7A, B; "Ker inferred"). The geothermal well sample from Hædarendi also appears to be in H_2O-CH_4 isotopic equilibrium around ~200°C (Fig. 7A), which is bracketed by the measured reservoir temperature of 170°C and gas temperature of 214°C (Table 4).

In contrast, CH_4 sampled from geothermal wells in Krafla and Námafjall shows D-disequilibrium in the H_2O-CH_4 system, with δD_{CH4} values ranging from -320 to -243‰, which are depleted by approximately 30 to 100‰ compared to the value expected for equilibrium at reservoir temperatures of ~250–300°C (Fig. 7A). There is an array of samples from the most D-depleted (Krafla well 32) to near-equilibrium (Krafla well 16) values (Fig. 7A). Isotopic disequilibrium in the H_2O-CH_4 pair is also observed for the Reykjanes well, with an apparent temperature of <200°C, compared to a reservoir temperature of 290°C (Fig. 7A, Table 4).

We note that the accuracy of the $\alpha_{H2O\text{-}CH4}$ thermometer is highly uncertain because this fractionation factor is derived by the combination of three fractionation factors, $\alpha_{H2O(g)\text{-}H2(g)}$ (e.g. Suess, 1949), $\alpha_{H2O(l)\text{-}H2O(g)}$ (Horita and Wesolowski, 1994) and $\alpha_{CH4(g)\text{-}H2(g)}$ (Horibe and Craig, 1995). The compounded error (1σ) of these fractionation factors is shown as grey shading in Fig. 7B, and illustrates that for a given α value the possible temperature range (within the 1σ uncertainty) spans ~100°C, notably in the 250–374°C range, where the temperature sensitivity of $\alpha_{H2O\text{-}CH4}$ is greatly reduced. Since $\alpha_{H2O\text{-}CH4}$ is simply a small difference between two larger numbers ($\alpha_{H2O\text{-}H2}$ and $\alpha_{CH4\text{-}H2}$), its uncertainty is large relative to its small variations in magnitude. For example, $\alpha_{H2O\text{-}CH4}$ ranges from 1.154 at 200°C to 1.123 at 400°C (Horibe and Craig, 1995), while $\alpha_{H2O\text{-}H2}$ ranges from 1.977 to 1.469 and $\alpha_{CH4\text{-}H2}$ from 1.719 to 1.304 over the same temperature interval. It must also be noted that the equilibrium line, based on the calibration by Horibe and Craig (1995), relies on the $\alpha_{H2O(g)\text{-}H2(g)}$ fractionation factor derived by Suess (1949), but that use of other $\alpha_{H2O(g)\text{-}H2(g)}$ relationships (e.g. Bardo and Wolfsberg, 1976; Cerrai et al., 1954) would yield different curves (dashed lines in Fig. 7B). Furthermore, another source of uncertainty arises from the calibration of the δD_{CH4} scale against the VSMOW reference scale as this requires measurement of δD values of reference H_2O and CH_4 at high precision. However, these differences are small compared to

the measured H_2O–CH_4 fractionations of ~100–300‰ (Fig. 7A) and do not change the nature of our interpretations.

5.1.3. Clumped isotopologue distributions

In comparison to the wide range of δD_{CH4} values, $\Delta^{13}CH_3D$ signals of methane are largely homogeneous (0.82 ± 0.34 to 1.77 ± 0.34‰), and correspond to apparent equilibrium temperatures ranging from 278 to 490°C (Fig. 4). If $\Delta^{13}CH_3D$ signals reflect methane formation or secondary equilibration temperature, the inferred temperatures would significantly exceed the thermogenic gas window of ~150 to 220°C typical of sedimentary basins (e.g. Quigley and Mackenzie, 1988; Stolper et al., 2017).

Among measured samples, well samples from Krafla and Námafjall yielded lower $\Delta^{13}CH_3D$ values with an average (±1 s.d.) $T_{\Delta^{13}CH_3D} = 438^{+55}_{-45}$°C, compared to the rest of the samples, which have generally higher $\Delta^{13}CH_3D$ values with an average (±1 s.d.) $T_{\Delta^{13}CH_3D} = 349^{+44}_{-37}$ °C (Table 2). While the four well samples from the Krafla and Námafjall area have a narrow $\Delta^{13}CH_3D$ range pointing to the highest apparent clumped temperatures, they exhibit a large range in δD_{CH4} that indicates pronounced departures from isotopic equilibrium against H_2O (Fig. 7B). We suggest that sample Krafla well 32, which has the lowest δD_{CH4}, $\delta^{13}C_{CH4}$ and $\Delta^{13}CH_3D$ values, represents a kinetic end-member, and that the array of data from Krafla and Námafjall reflects different degrees of equilibration from initial kinetic methane (Fig. 5C and Fig. 7A, B). Methane from geothermal wells at Reykjanes and Hædarendi also has $\Delta^{13}CH_3D$ values which do not correspond to measured reservoir temperature (Fig. 5C) and the $1000\ln\alpha_{H2O\text{-}CH4}$ geothermometer (Fig. 7B). In contrast, samples from Nisyros and Kerlingarfjöll have $\Delta^{13}CH_3D$ values which generally agree with the apparent equilibrium temperatures obtained from $\alpha_{H2O\text{-}CH4}$ (Fig. 7B), suggesting that they represent equilibrium end-member methane. We examine the rates of deuterium exchange and isotopic equilibration to explain δD_{CH4} and $\Delta^{13}CH_3D$ variability in section 5.3.1.

5.1.4. ^{13}C fractionation between CO_2 and CH_4

Similar trends of equilibrium and disequilibrium methane are observed in ^{13}C-fractionation between CO_2–CH_4, where the most negative $\delta^{13}C_{CH4}$ values observed at Krafla, Námafjall and Reykjanes are associated with disequilibrium (i.e. kinetic) signals, while CH_4 from Nisyros and Kerlingarfjöll appears to show equilibrium signals relative to $\Delta^{13}CH_3D$, with apparent isotopic temperatures from 300 to 350°C (Fig. 7C, D). Variations in the fractionation factor $\alpha_{CO2\text{-}CH4}$ are primarily due to variations in $\delta^{13}C_{CH4}$, since $\delta^{13}C_{CO2}$ is relatively constant for all samples from Iceland ($\delta^{13}C_{CO2}$ = -2.4 to -3.8‰) and Nisyros ($\delta^{13}C_{CO2}$ = -0.8 to -1.9‰). While the CO_2-CH_4 apparent isotopic temperatures (Fig. 7C) at Krafla and Námafjall are not so far from reservoir temperatures between ~250-290°C (e.g. Fig. 5, Table 4), we qualify them as being in disequilibrium relative to the $\Delta^{13}CH_3D$ geothermometer which indicates temperatures of 438^{+55}_{-45}°C. In contrast, the sample from Hædarendi, which is a high CO_2-producing well (Table 1), shows simultaneous apparent equilibrium between the $1000\ln\alpha_{CO2\text{-}CH4}$ and $\Delta^{13}CH_3D$ geothermometers at a temperature of ~300°C, which is however significantly hotter than the hydrothermal reservoir temperature of 200°C.

The relatively narrow range in $\delta^{13}C_{CH4}$ values of Krafla and Námafjall well samples, from -39.6‰ to -35.8‰, compared to their large δD_{CH4} range from -320‰ to -243‰, is consistent with pyrolysis of terrestrial xylite, according to the fractionation factors derived by Berner et al. (1995). However, the two Krafla samples are farthest from each other in δD_{CH4} space but closest to each other in $\delta^{13}C_{CH4}$ space (Fig. 7A, C), which could mean that while the CH_4 generation process may lead to disequilibria in both $\delta^{13}C_{CH4}$ and δD_{CH4}, mechanisms controlling D and ^{13}C isotopic equilibration are different. Alternatively, this observation could reflect slight variations in the isotopic composition of source organics. Since the mechanism of carbon isotope exchange between CO_2 and CH_4 is not well understood (e.g. McCollom, 2013) and indeed its use as a geothermometer for natural systems has been put into question (Fiebig et al., 2019), ^{13}C fractionations must be interpreted with caution. Therefore, while CH_4 from Nisyros, Kerlingarfjöll and Hædarendi appears to show simultaneous $\Delta^{13}CH_3D$ and $\alpha_{CO2\text{-}CH4}$ equilibrium, we must discuss the rates of isotopic exchange (c.f. section 5.3.2) to assess whether this reflects "true" attainment of equilibrium.

5.2. Expected isotopologue signals of thermogenic and abiotic methane

In the previous section, we identified equilibrium and kinetic end-member methane, the latter characterized by low δD_{CH4} and $\Delta^{13}CH_3D$ values. Here, we discuss whether $\Delta^{13}CH_3D$ values of "kinetic" methane can place constraints on a thermogenic versus abiotic origin. Disequilibrium $\Delta^{13}CH_3D$ signals have been measured for methane generated in laboratory experiments via thermal cracking of organic matter (Shuai et al., 2018a). Other experiments that produced methane through abiotic reactions (Young et al., 2017) have also shown strong $\Delta^{12}CH_2D_2$ disequilibria along with minor $\Delta^{13}CH_3D$ disequilibria. The high apparent temperatures associated with 'kinetic' methane at Krafla could thus reflect disequilibrium isotopologue signals from either thermogenic or abiotic methane (Fig 1, yellow ovals). On the other hand, the geothermal systems at Krafla and Námafjall are characterized by steep geothermal gradients, due to the active Krafla magma chamber at a depth of just over 2 km. While the $\Delta^{13}CH_3D$-based temperature of 438^{+55}_{-48}°C obtained for sampled wells is higher than reservoir temperatures of ~250-300°C, it is indistinguishable from the temperature of ~440°C measured in fluids at a ~2 km depth during drilling of the IDDP-1 well (Elders et al., 2014; Scott et al., 2015; Heřmanská et al., 2019). Hence, methane could be sourced from a deep superheated reservoir in close vicinity to the magmatic heat source, either thermogenically or abiotically (Fig. 1, red ovals). In any case, if the high apparent clumped temperatures are the result of kinetic processes, these effects may be relatively small, since high temperatures are prevailing in this geothermal system.

5.2.1. Isotopologue signals for thermogenic methane

Thermogenic methane produced in sedimentary basins peaks at temperatures between 150 and 220°C (e.g. Quigley and Mackenzie, 1988; Tissot and Welte, 1978). Methane from thermogenic natural gas deposits tends to yield clumped temperatures that usually agree with independently constrained gas formation temperatures (Ono et al., 2014; Stolper et al., 2014a; Wang et al., 2015; Stolper et al., 2017; Shuai et al., 2018b). In addition, thermogenic methane

from hydrothermally heated sediments at Guaymas Basin (Wang et al., 2015) and Juan de Fuca Ridge (Douglas et al., 2017) yielded temperatures of 326°C and 305 to 365°C, respectively, consistent with measured vent fluid temperatures. However, non-equilibrium isotopologue signatures are implied in some unconventional oil-associated reservoirs (Douglas et al., 2017), with derived $T_{\Delta_{18}}$ exceeding 200°C, the estimated maximum temperature for oil stability under geological timescales (e.g. Hunt, 1996).

Shuai et al. (2018a) investigated the clumped isotopologue signals of experimentally produced thermogenic CH_4 by subjecting coal and shale to pyrolysis at temperatures from 380 to 620°C. Both series of experiments were characterized by near-equilibrium signatures during the early stages of thermal cracking, followed by departures from isotopologue equilibrium with increasing temperatures, in which lower-than-expected Δ_{18} values were produced. This led the authors to suggest that CH_4 generated by secondary cracking of C_{2-5} hydrocarbons can carry clumped isotopologue signatures characterized by pronounced kinetic isotope effects. These experimental results suggest that kerogen cracking produces methane in clumped isotopologue equilibrium, possibly due to local reversibility in hydrogen exchange, whereas cracking of alkyl groups from oil or C_{2+} gases irreversibly generates methane with non-equilibrium clumped signatures (Shuai et al., 2018a).

The conditions that may lead to thermogenic methane generation in hydrothermal systems are quite different from the "dry" experimental conditions investigated by Shuai et al. (2018a), and may thus evoke a different clumped pattern. While these pyrolysis experiments used shale and coal as starting organic materials, thermal cracking in Icelandic hydrothermal fluids is thought to occur principally via the breakdown of organic matter transported to depths by external waters, since no organic sediments are present in these systems (Fiebig et al., 2019). In this respect, the starting organic matter would either represent or be derived from DOC and POC. Moreover, the most pronounced kinetic effects observed by Shuai et al. (2018a) occur when the ratio of C_{2-5}/C_{1-5} decreases between 0.1 and 0.01 (or as C_1/C_{2-5} increases from ~10^1 to 10^2), followed by a return to equilibrium as this ratio goes beyond 10^2. The measured C_1/C_{2+} ratios in our hydrothermal fluids fall within the range 10^2–10^4 (Table 1), and could therefore be more analogous to the highest thermal maturities in the experiments of Shuai et al. (2018a) associated with equilibrium clumped signatures. Additionally, the non-equilibrium effects shown by the experiments of Shuai et al. (2018a) co-evolve with increases in δD and δ^{13}C values, mirroring increases in thermal maturity. In contrast, such correlation is not observed with the $\Delta^{13}CH_3D$ values measured in Krafla and Námafjall well fluids, which remain uniformly low over ranges of ~80‰ in δD and ~5‰ in δ^{13}C values similar to those observed by Shuai et al. (2018a) (Fig. 7B, D). Nonetheless, Krafla and Námafjall may be characterized by fast recharge of fluids and input of immature, low-δ^{13}C organic matter, which could produce thermogenic CH_4 with non-equilibrium $\Delta^{13}CH_3D$ values, though the magnitude of such kinetic process cannot be evaluated.

5.2.2 Isotopologue signals for abiotic methane

Abiotic methane can be produced by a variety of processes and under a wide range of temperatures and pressures, as demonstrated in a growing number of laboratory experiments (Fu et al., 2007; McCollom et al., 2010; Taran et al., 2010; McCollom, 2013). It is expected that

abiotic methane formed by different processes and carbon sources should carry different isotopologue signatures. In natural settings, methane of potentially abiotic origin seems to have higher $\delta^{13}C$ values compared to conventional biogenic and thermogenic methane, but its δD values largely overlap with these conventional sources (Fig. 3; Reeves and Fiebig, 2020).

Compared to the wide range of $\delta^{13}C$ and δD values of proposed abiotic methane (Fig. 3), methane from non-sedimented seafloor hydrothermal vents tends to carry homogeneous isotope and isotopologue signals, with $\delta^{13}C$, δD, and $\Delta^{13}CH_3D$ values ranging from -11 to -18‰, -98 to -127‰, and 0.95 to 3.0‰, respectively, with $\Delta^{13}CH_3D$ values above 1.85‰ only observed at the Lost City hydrothermal field (Proskurowski et al., 2008; Wang et al., 2018; Labidi et al., 2020). These relatively uniform isotopologue signals suggest a common origin for methane associated with seafloor hydrothermal vents, proposed to be fluid trapped as fluid inclusions in the oceanic lithosphere (Kelley, 1996; Wang et al., 2018; Klein et al., 2019; Labidi et al., 2020). The kinetic end-member CH_4 measured in this study (Krafla-32) is significantly more depleted in $\delta^{13}C$ and δD than CH_4 from seafloor hydrothermal vents (even when correcting for the ~80‰ shift between Iceland meteoric water and VSMOW; see Fig. 7A), suggesting that the generation processes of methane for Krafla-32 are different from those of abiotic CH_4 from seafloor vents.

Experimental studies of abiotic methane generation have shown that produced hydrocarbons, including CH_4, are depleted in ^{13}C compared to the initial carbon source, but the magnitude of the fractionation varies (McCollom, 2013 and references therein). For instance, Taran et al. (2010) carried out open-system Fischer-Tropsch-type (FTT) synthesis of CH_4 via the hydrogenation of CO_2 on iron and cobalt catalysts at 350 and 245°C, respectively, and observed ^{13}C fractionation of >40‰ between CO_2 and CH_4. Fu et al. (2007) carried out experiments of CO_2 reduction by H_2 in aqueous NaCl fluids using magnetite as a potential catalyst, at 400°C and 500 bars, and observed $\delta^{13}C$ isotopic fractionations between CO_2 and CH_4 from 4.6 to 27.1‰, whereas the value expected for equilibrium at 400°C is 19‰. They also reported relatively constant δD fractionation between H_2O–CH_4 of 214 to 229‰ (equilibrium = 132‰), with CH_4 having lower δD values than expected for equilibrium fractionation. Therefore, bulk isotopic signatures of abiotic CH_4 produced in the laboratory can exhibit significant variability and overlap with our kinetic end-member Krafla-32.

Young et al. (2017) investigated the clumped isotopologue signatures of abiotic methane produced by two different processes: 1) CH_4 generated via the Sabatier reaction (1) by reacting gaseous mixtures of CO_2 and H_2 with a Re catalyst at 70 and 90°C and 2) hydrolysis of silane ($Si_5C_{12}H_{36}$) at temperatures of 300 to 600°C and 100MPa. The product CH_4 in several experiments showed $\Delta^{13}CH_3D$ values that agreed with generation temperatures, although some experiments had $\Delta^{13}CH_3D$ deficits of up to ~1‰. Comparatively large deficits in $\Delta^{12}CH_2D_2$ values were observed, particularly for lower temperature experiments. Proposed abiotic methane from deep mine fluids in Precambrian shields (e.g. Sherwood Lollar et al., 2006; 1993) was also shown to carry lower-than-equilibrium $\Delta^{12}CH_2D_2$ signatures combined with equilibrium $\Delta^{13}CH_3D$ values, and could thus be produced similarly (Young et al., 2017). These observations suggest that $\Delta^{13}CH_3D$ signatures may be relatively insensitive to kinetics. The isotopologue systematics of hydrothermal CH_4 generation from CO_2 reduction, however, have not been studied, making it hard to evaluate whether CH_4 measured in this study carries abiotic signals.

The $\Delta^{12}CH_2D_2$ values reported for Nisyros steam vents (Gonzalez et al., 2019) and shown in Table 2 are slightly lower than expected for equilibrium with $\Delta^{13}CH_3D$ and point to higher apparent temperatures, thus they could reflect non-equilibrium processes similar to those described by Young et al. (2017). However, as we outline in the next section, the residence times of Nisyros fluids are thought to be long enough for $\Delta^{13}CH_3D$ signatures to equilibrate, and $\Delta^{12}CH_2D_2$ should equilibrate at least twice as quickly (Labidi et al., 2020), albeit with potentially more pronounced initial kinetic signals. Therefore, the $\Delta^{12}CH_2D_2$ deficits reported by Gonzalez et al. (2019) remain difficult to explain. However, we note that these deficits are small (on the order of 1‰) compared to the large kinetic signals (>10‰) exhibited by the experiments of Young et al. (2017) and could reflect uncertainty associated with sample preparation, which was not characterized.

5.3. Closure temperature of CH_4 in geothermal fluids

5.3.1 Isotopic exchange between H_2O and CH_4

In this section, we evaluate if observed isotopologue equilibrium and disequilibrium signals can be explained by different rates of isotope exchange reactions. Upon cooling of fluids, isotope exchange reactions that operate at faster rates are more likely to re-equilibrate at lower temperatures.

Ohmoto and Lasaga (1982) derived the following rate law for isotope exchange between chemical species X and Y:

$$\ln\left(\frac{\alpha^e - \alpha}{\alpha^e - \alpha^0}\right) = \ln(1 - F) = -k([\mathrm{X}] + [\mathrm{Y}])t \qquad (4a)$$

where α^e, α^0 and α are the isotope fractionation factors at equilibrium, at time 0 and time t, respectively; F is the fraction of isotopic exchange (or progress variable); k is the second order rate constant (e.g. units in $cm^3\ mol^{-1}\ s^{-1}$); [X] and [Y] are concentrations of reactants (such as H_2O and CH_4) and t is time. Equation (4a) shows that the rate of isotope exchange depends upon the sum of the two reactants. This concentration dependence is important for CH_4/H_2 and CO_2/CH_4, where the rate of exchange is limited by the collision of two chemical species. However, when considering isotope exchange with H_2O (H_2O-CH_4 and H_2O-H_2), we can assume that H_2O is an infinite reservoir, and equation (4a) reduces to:

$$\ln\left(\frac{\alpha^e - \alpha}{\alpha^e - \alpha^0}\right) = -k't \qquad (4b)$$

where $k' \simeq k[H_2O]$ is the pseudo first order rate constant (e.g. in units of yr^{-1}). The same rate law was derived by Pester et al. (2018) for D/H exchange between H_2O and H_2.

If the methane isotopologue exchange reaction proceeded via internal equilibration (e.g. Table 3), then $k' = k([^{12}CH_4 + {}^{12}CH_3D] + [{}^{13}CH_4 + {}^{13}CH_3D]) \simeq k[CH_4]$, and the overall isotopologue exchange rate would be proportional to $[CH_4]$. That is, a faster exchange rate would be expected when CH_4 concentration is higher. This is understood as the frequency of CH_4 to CH_4 collisions increases as the square of the concentration of CH_4. This type of exchange has been suggested by recent studies evaluating the kinetics of dual clumped CH_4 isotope bond reordering (Labidi et

al., 2020; Giunta et al., 2021). Methane isotopologue equilibration in water-dominated systems, however, likely proceeds by D/H exchange with water via the two separate reactions:

$$^{12}CH_3D + H_2O \rightleftharpoons {}^{12}CH_4 + HDO \quad (5)$$

$$^{13}CH_3D + H_2O \rightleftharpoons {}^{13}CH_4 + HDO \quad (6)$$

In this case, $k'=k[H_2O]$, and the isotopologue exchange rate becomes independent of CH_4 concentration.

Based on experiments performed at different temperatures (e.g. Koepp, 1978; Reeves et al., 2012), Wang et al. (2018) derived an empirical rate law to describe this exchange as:

$$\log k' = 15.247 - \frac{9994.7}{T} \quad (7)$$

where k' is in yr^{-1}, and T is temperature in Kelvin. This rate law corresponds to a relatively high activation energy of 191 kJ/mol.

We propose that the elementary reactions that characterize D/H isotope exchange for methane involve H-abstraction from CH_4 by H radicals (reaction 8). The product methyl radical quickly reacts with H_2O to form CH_4 and an OH radical (reaction 9).

$$CH_4 + {}^{\bullet}H \rightarrow {}^{\bullet}CH_3 + H_2 \quad (8)$$

$${}^{\bullet}CH_3 + H_2O \rightarrow CH_4 + {}^{\bullet}OH \quad (9)$$

The activation energy for reaction (8) is 88 kJ/mol (Sutherland et al., 2001). The high apparent activation energy of 191 kJ/mol — based on equation (7) — suggests that the overall exchange rate could be limited by radical initiation reactions such as:

$$H_2O \rightarrow {}^{\bullet}H + {}^{\bullet}OH \quad (10)$$

$$H_2 \rightarrow 2{}^{\bullet}H \quad (11)$$

These reactions are highly endothermic, with enthalpies of reactions of 505 and 441 kJ/mol at 700K for (10) and (11), respectively (GRI-Mech 3.0 - Smith et al., 2000), which may partly explain the high activation energy of 191 kJ/mol of the D/H exchange reactions (reactions (5) and (6)). The formation of such radicals could be catalyzed by rock surfaces, aided by opening of fractures in tectonically active environments and by the electrical conductivity of water (Kita et al., 1982; Balk et al., 2009). Under geothermal conditions, HS radicals could also be important in abstracting H from CH_4. This may also have been the case for the experiments of Reeves et al. (2012), which were used to establish the rate law for D/H exchange between CH_4 and H_2O (Eq. 7), since they were carried out at the pyrite-pyrrhotite-magnetite buffer.

We used equation (7) to model the evolution of methane isotopologue ratios ($\Delta^{13}CH_3D$ and δD) with a starting isotopic composition corresponding to our kinetic end-member Krafla well 32 (15-AS-07), with δD_{CH4} = -319.6‰, δD_{H2O} = -82.4 ‰ (1000ln$\alpha_{H2O\text{-}CH4}$ = 300‰) and $\Delta^{13}CH_3D$ = 0.82‰. We use this sample as an end-member since it has the lowest δD, $\delta^{13}C$ and $\Delta^{13}CH_3D$ signatures among measured samples in this study. We also note that this δD_{CH4} value is at the lower end of geothermal samples reported by Fiebig et al. (2019) (see Fig. 7A) and is therefore our best estimate for the kinetic end-member. However, as outlined below, the nature of our interpretations does not change if we use a different end-member, e.g. with lower δD_{CH4} and $\Delta^{13}CH_3D$.

Isotopic fractionation according to reactions (5) and (6) can be described by:

$$^{12}\alpha_{H2O-CH4} = \frac{[^{12}CH_4] \cdot [HDO]}{[^{12}CH_3D] \cdot [H_2O]} \quad (12)$$

$$^{13}\alpha_{H2O-CH4} = \frac{[^{13}CH_4] \cdot [HDO]}{[^{13}CH_3D] \cdot [H_2O]} \quad (13)$$

Similarly, the CH_4 clumped isotopologue distribution (see Table 3 for the isotope exchange reaction) can be written as:

$$Q = \frac{[^{13}CH_3D] \cdot [^{12}CH_4]}{[^{12}CH_3D] \cdot [^{13}CH_4]} \quad (14)$$

Hence, it follows that:

$$Q = {}^{12}\alpha / {}^{13}\alpha \quad (15)$$

We assume in our calculations that the equilibrium $\alpha_{H2O\text{-}CH4}$ relationship derived by Horibe and Craig (1995) (Table 3) corresponds to $^{12}\alpha_{eq}$ values since the abundance of $^{12}CH_4$ is two orders of magnitude higher than $^{13}CH_4$. Then, $^{13}\alpha_{eq}$ is calculated from $^{12}\alpha_{eq}$ and K_{eq}, the value of Q representing clumped isotopologue equilibrium, using equations (2) and (3). Therefore, we model the evolution of $^{12}\alpha$, $^{13}\alpha$ and Q, at different temperatures following equations (4b), (7) and (15), and starting from the end-member composition (Krafla-32), as well as from an arbitrary end-member with more pronounced disequilibrium (1000ln$\alpha_{H2O\text{-}CH4}$ = 400‰ and $\Delta^{13}CH_3D$ = 0‰). The resulting calculations are reported in Table S1 and illustrated in Figures 7B and 8A, B. Equilibration paths are shown for temperatures of 450°C, 350°C and 250°C. This allows us to explore the equilibration timescales of methane isotopologues across a range of hydrothermal conditions. It is worth noting that the above equations imply that equilibration of δD_{CH4} and $\Delta^{13}CH_3D$ occur through the same mechanisms and thus have the same timescales. Therefore, equilibration paths shown in Figure 7B are nearly straight lines. Equations 4b and 7 also imply that the timescale of equilibration will be the same for a given temperature regardless of the initial extent of disequilibrium (Fig. 8A, B).

Equilibration at 350°C, for example in the geothermal reservoir at Nisyros, is expected to be achieved within 10-100 years, which is consistent with the observation that CH_4 at Nisyros is in isotopologue equilibrium, considering that the last hydrothermal eruption, which may have introduced disequilibrium in the deep permeable zone, occurred more than 100 years ago (Marini et al., 1993). Figures 8A, B also show that at 250°C, there should be virtually no isotopic

exchange occurring at timescales relevant for this study (<1000 years), thus any methane formed or entrained into the subcritical hydrothermal reservoirs of all of the Icelandic geothermal systems studied here, which have reservoir temperatures of 250–300°C (Table 4), should retain its initial isotopologue ratios. Therefore, apparent H_2O-CH_4 isotopic equilibrium at the reservoir temperature of ~200°C in the Hædarendi well is unlikely to reflect true attainment of equilibrium. Radium isotopes have been used to estimate fluid residence times of <5 years in Reykjanes wells (Kadko et al., 2007), which would not be sufficient for H_2O-CH_4 isotopic equilibrium to be attained at the reservoir temperature of 290°C (Fig. 8A, B). This can explain the observation that $\Delta^{13}CH_3D$ and $\alpha_{H2O\text{-}CH4}$ are not in mutual equilibrium for the Reykjanes well (Fig. 7B). The apparent $\Delta^{13}CH_3D$-based temperature for this well is 379^{+37}_{-32}°C, which could represent a kinetic signal from methane formation in the hydrothermal reservoir, but could also imply methane formation in deeper, hotter parts of the geothermal system which have been characterized by deep drilling (e.g. Bali et al., 2020).

At 450°C, which could represent a superheated vapor phase in the vicinity of magmatic intrusions at Krafla and Námafjall (Elders et al., 2014; Heřmanská et al., 2019), equilibration of δD_{CH4} and $\Delta^{13}CH_3D$ values is expected to occur within days to one month (Fig. 8A, B). Therefore, if methane is generated in such phase, the superheated vapors must rapidly ascend into the overlying ~250-300°C subcritical reservoir (e.g. Figs. 1, 6) to preserve the observed range of disequilibrium δD_{CH4} values. Further equilibration at reservoir temperatures would likely proceed more slowly than fluid residence times of ~5-50 years (e.g. Stefánsson et al., 2015). Hence, if the range of δD_{CH4} values for Krafla and Námafjall reflects high-temperature equilibration in a superheated vapor phase, the $\Delta^{13}CH_3D$ value of kinetic end-member Krafla-32 actually closely records the expected high temperature of superheated vapor. This would imply that CH_4 is formed with near-equilibrium $\Delta^{13}CH_3D$ signatures but pronounced δD_{CH4} deficits. However, it is also possible that CH_4 forms at reservoir temperatures of 250–300°C with both kinetic δD and small $\Delta^{13}CH_3D$ deficits, which would be preserved due to slow kinetics. The range in δD_{CH4} values of Krafla and Námafjall samples would in this case be explained by varying thermal maturity of degrading organic matter.

5.3.2. Rates and mechanisms of carbon isotopic exchange between CH_4 and CO_2

The rates and mechanisms of chemical and isotopic equilibration between CH_4 and CO_2 (1) are poorly constrained but thought to be much slower than the D/H isotope exchange between CH_4 and H_2O (Giggenbach, 1997; Cole and Chakraborty, 2001). While overall isotopic exchange can be represented by the ^{13}C exchange reaction shown in Table 3, Giggenbach (1997) points out that this reaction is unlikely since it requires a complete rearrangement of two C=O bonds and four C–H bonds between reacting CO_2 and CH_4 molecules. By analogy to the mechanism of S-isotope exchange between H_2S and H_2SO_4 proposed by Ohmoto and Lasaga (1982), carbon isotope exchange between CH_4 and CO_2 could proceed via two-carbon intermediate species such as acetic acids from a series of reactions such as association (16), intramolecular C-isotope exchange (17), or dissociation reactions (18) (Blake and Jackson, 1969; Mackie and Doolan, 1984; Duan and Page, 1995):

$$^{13}CO_2 + {}^{12}CH_4 \rightarrow {}^{12}CH_3{}^{13}COOH \quad (16)$$

$$^{12}CH_3{}^{13}COOH \rightleftharpoons {}^{13}CH_3{}^{12}COOH \quad (17)$$

$$^{13}CH_3{}^{12}COOH \rightarrow {}^{13}CH_4 + {}^{12}CO_2 \quad (18)$$

While an experimental study by Dias et al. (2002) demonstrated that C-isotope exchange between CO_2 and the carboxylic group of acetic acid occurs at a reasonable rate, the rate for intramolecular C-isotope exchange (17) is expected to be slow and likely to be the rate limiting step.

Another potentially important mechanism for the C-isotope system is exchange of C between CH_4 and organic matter. Sackett (1993) reported on a pyrolysis experiment demonstrating that C-isotope exchange between kerogen and CH_4 at 700°C is completed in about 200 hours, corresponding to a half-exchange timescale of ~40h. Using the Arrhenius relationship, we can calculate that at 400°C this would be about half a year. The exchange rate in natural settings would depend upon the reactive surface area of organics and is therefore difficult to estimate, but we expect that this process could be relevant at Nisyros, where the basement rocks include cretaceous limestone (Marini et al., 1993), which could provide kerogen that would exchange C isotopes with methane .

A third mechanism of C-isotope exchange could be via partial chemical equilibration between CO_2 and CH_4 following reaction (1), such as:

$$^{12}CO_2 + 4H_2 \rightleftharpoons {}^{12}CH_4 + 2H_2O \quad (19)$$

$$^{13}CO_2 + 4H_2 \rightleftharpoons {}^{13}CH_4 + 2H_2O \quad (20)$$

(e.g. Fiebig et al., 2004; Giggenbach, 1997). As outlined earlier, the rates for this reaction are poorly known. Early experiments by Berndt et al. (1996) suggested a reduction of 1% CO_2 during serpentinization of olivine at 300°C in a period of about two months, from which the forward rate could be calculated. However, more recent experiments using a more robust ^{13}C-labelling technique (McCollom, 2016) showed that rates are likely much slower, and that many previous experimental work invoking abiotic reduction of inorganic carbon compounds may have been affected by background concentrations of reduced carbon, potentially from the reacting minerals. The experiments of McCollom (2016) failed to produce any significant ^{13}C-labelled methane despite having a high thermodynamic drive for reaction (20) (i.e. high fH_2), except for one experiment where a separate vapor phase was allowed to form.

In geothermal systems fH_2 depends on a ladder of reactions involving hydrolysis and progressive oxidation of Fe^{2+} to Fe^{3+}, which in turn depend on fluid pH, on the chemical composition of the surrounding rocks (e.g. mafic vs felsic) and on the stability of secondary minerals formed (Stefánsson, 2017). In general, this provides much lower thermodynamic drive for CO_2 reduction than those expected in serpentinization environments. Nevertheless, we use the ^{13}C-labelled experiment of McCollom (2016) where some CH_4 was produced as an upper estimate for the rates of chemical equilibration between CO_2 and CH_4. This experiment was conducted at 300°C and found that 52 μmol/kg of $^{13}CH_4$ was produced over 3885h, with a final ΣCO_2 of 11mmol/kg. From this we derive a pseudo-first-order rate constant k_c' of 0.001 a^{-1}

(where $k_c' = \ln\left(\frac{c_0}{c_t}\right)/t$), which is about 60 times slower than the rate calculated from the Berndt et al. (1996) experiments.

Giggenbach (1997) suggested that ^{13}C isotope exchange is slower than chemical exchange by a factor of ~400. We apply the same approach to derive the following pseudo-first-order rate constants of chemical (k_c') and isotopic exchange (k_i'):

$$\log k_c' = 4.77 - 4440/T \quad (21)$$

$$\log k_i' = 2.16 - 4440/T \quad (22)$$

where the second term is based on a previously determined activation energy for the Fischer-Tropsch process of ~85 kJ/mol (Huff and Satterfield, 1984; Zimmerman and Bukur, 1990).

These rates are substituted into equation (4b) to compute progressive equilibration of $\alpha_{CO2\text{-}CH4}$ values. While the reaction order is likely different, for the sake of comparison with H_2O-CH_4 exchange we make the simplifying assumption that k_c' and k_i' are the overall pseudo-first order rate constants and that the equation $\ln(1-F) = -k't$ (4b) is still valid. Progressive isotopic equilibration according to equations (22) and (4b) is shown in Fig. 7D and 8C using the same end-member as in the deuterium exchange calculations (Krafla well 32). From this it is clear that rates of ^{13}C exchange are expected to be much slower than those of D exchange at high temperature, and are reflected by unreasonably long timescales for any ^{13}C equilibration to occur in the Icelandic systems studied, and in Nisyros provided that chemical and isotopic disequilibrium was likely introduced by the 1873 eruption (Fig. 7D, 8C). Therefore, it appears that if any ^{13}C isotopic exchange occurred, such as implied by the apparent equilibrium $\alpha_{CO2\text{-}CH4}$ values observed at Nisyros, Kerlingarfjöll and Hædarendi (Fig. 7D), then CO_2 reduction must be catalyzed by either sedimentary organic material or acetic acids as discussed earlier. Alternatively, the apparent ^{13}C isotopic equilibrium is coincidental in these systems and reflects the ^{13}C-enrichment trend associated with open-system breakdown of organic matter. In its advanced stage, the latter process could generate methane having an isotopic composition consistent with equilibrium-like $\delta^{13}C_{CH4}$ values (Fiebig et al., 2019).

5.4. Process of CH_4 generation and equilibration

Overall, the kinetic end-member CH_4 isotopologue composition of Krafla-32 is consistent with thermogenic methane produced by thermal cracking of organic material at various possible temperatures (Fig. 8A, B). For example, CH_4 generated in the hydrothermal reservoir at ~250°C would preserve any kinetic fractionations associated with thermal cracking. However, the trend from low δD_{CH4} values towards equilibrium at Krafla is well reproduced by partial isotopologue equilibration (Fig. 7A, B), and this equilibration process appears to be associated with high-enthalpy wells (Fig. 9). Such wells have a high vapor/liquid ratio, which could indicate the addition of superheated vapor to the subcritical reservoir (Elders et al., 2014). The input of superheated vapor is supported by the observation of a partially equilibrated acid well with high enthalpy (Fig. 9), which is thought to represent condensed superheated vapor (Heřmanská et al., 2019). Therefore, low $\Delta^{13}CH_3D$ values observed in Krafla could instead represent a unique window into the fluid processes occurring in the deep roots of geothermal systems.

Fluid flow in a hydrothermal reservoir is largely controlled by host rock permeability and by the thermal structure of the geothermal system, which is in turn determined by their magmatic history (Hayba and Ingebritsen, 1997; Fournier, 1999; Scott et al., 2016). Numerical simulations show that the extent of boiling zones is controlled by both magmatic emplacement depth and host rock permeability: for example, boiling zones are restricted to shallow levels (≤1km) in systems with high permeability (≥10^{-14} m^2), whereas they may span the whole depth range from surface to intrusion in systems with intermediate permeability (~10^{-15} m^2), provided that the intrusion depth is <3 km (Scott et al., 2016). These conditions are optimal for the development of supercritical geothermal resources, as observed in the Krafla geothermal system where the intrusion depth is just over 2 km (Scott et al., 2015). Therefore, the observation of kinetic CH_4 at Krafla and Námafjall with $\Delta^{13}CH_3D$-based temperatures (438^{+55}_{-45}°C) corresponding to the temperatures of superheated vapor sampled by the IDDP-1 well (Elders et al., 2014) could reflect the recent magmatic history of the geothermal system, shallow depth to magmatic bodies and appropriate host rock permeability (Fig. 10A).

Local variations in host-rock permeability, for example due to its temperature dependence near the magmatic intrusion (e.g. Hayba and Ingebritsen, 1997; Fournier, 1999) may control the extent of H_2O-CH_4 isotopic exchange, since it would affect fluid velocities and thus, residence times. For example, Krafla well 32 (kinetic end-member CH_4) could sample a zone where host-rock permeability is slightly higher, which would promote faster recharge of meteoric fluids with liquid enthalpy and quenching of kinetic CH_4 isotopologue signals. In contrast, high-enthalpy wells may sample zones with lower host-rock permeability, which could provide more favorable conditions for the development of more extensive and longer-lived "pockets" of superheated vapor where CH_4 isotopologue equilibration proceeds over longer durations (Fig. 10A). Hence, the unique thermal structure of the Krafla geothermal system, where conditions leading to supercritical geothermal resource formation are optimized (Scott et al., 2015), could in large part be responsible for the unique CH_4 isotopologue signals observed there (Fig. 7B).

In contrast, the other systems studied here (Reykjanes, Kerlingarfjöll, Nisyros) have older magmatic histories (~100-1000 years) and deeper heat sources (~3-5 km) (e.g. Ármannsson, 2016; Bachmann et al., 2012; Bali et al., 2020; Caliro et al., 2005) where supercritical fluids may not be as important, or not present at all (Scott et al., 2016). This could in part explain their systematically higher $\Delta^{13}CH_3D$ values, whereas the degree of H_2O-CH_4 isotopic equilibration will be determined by reservoir temperature and fluid residence times. Nisyros can be characterized as an equilibrium CH_4 isotopologue end-member, with all geothermometers pointing to reservoir temperatures of 350°C (e.g. Fig. 5C and 7). Host rock permeability in this system is characterized by two permeable zones separated by an aquiclude (Chiodini et al., 1993; Marini et al., 1993), and thus fluid residence times are longer, probably on the order of 100-1000 years. Figure 8 shows that this is largely sufficient for $\Delta^{13}CH_3D$ and δD_{CH4} isotopologue equilibrium to be attained, but probably not for CO_2-CH_4 isotopic equilibrium. A schematic representation is shown in Fig. 10B.

Organic matter in small concentrations brought from the surface may reach the roots of geothermal systems without breaking down significantly. As fluids approach the heat source thermogenic breakdown would become more effective. This is analogous to CH_4 generation during pyrolysis experiments conducted over short timescales, which is commonly optimized at temperatures above 400°C (Littke et al., 1995; Shuai et al., 2018a). The thermal cracking

generates methane with disequilibrium δD and $\delta^{13}C$ signals, which may be exemplified by samples from the Krafla and Námafjall areas, where these signals are preserved as superheated vapors are rapidly quenched in the overlying reservoirs. The difference in isotopologue signals from other locations could reflect the absence of substantial supercritical resources and/or longer fluid residence times. Alternatively, thermogenic breakdown may occur in shallower regions of the hydrothermal reservoirs, with low $\Delta^{13}CH_3D$ values mostly reflecting kinetic effects associated with breakdown of organic matter at hydrothermal reservoir temperatures. The lower reservoir temperatures of Icelandic systems (Table 4) would limit the extent of H_2O-CH_4 isotopic exchange and thus favor the preservation of kinetic signals, while the higher temperatures at Nisyros could lead to isotopic and isotopologue equilibration. However, we consider this latter scenario less likely, since it requires the preservation of large δD_{CH4} kinetic signals with invariant $\Delta^{13}CH_3D$ signals for Krafla and Námafjall samples.

Because isotopologue signals for CH_4 produced from CO_2 reduction in hydrothermal settings are not well characterized, we also cannot exclude the possibility of a contribution of abiotic methane. The low $\Delta^{13}CH_3D$ values raise the interesting possibility that methane could be produced abiotically in the supercritical reservoir at Krafla, at temperatures as high as 490°C. Such high temperatures and reactions in a superheated vapor phase could overcome the kinetic barriers associated with CO_2 reduction (McCollom, 2013; Reeves and Fiebig, 2020). It is also interesting to note that locations where CO_2 flux is particularly high, such as Nisyros (Bini et al., 2019) and Hædarendi (Ármannsson, 2016), also have higher concentrations of CH_4 (Table 1) in simultaneous apparent clumped and ^{13}C equilibrium, suggesting possible high-temperature ^{13}C isotopic exchange. Our model of CH_4 generation at Krafla and Námafjall (Fig. 10A) suggests a decoupled origin for methane and the bulk of the geothermal fluids. This is reminiscent of the interpretations of CH_4 isotopologues in seafloor vents, where most CH_4 is thought to be produced in fluid inclusions and picked up by actively circulating hydrothermal fluids. There again, low $\Delta^{13}CH_3D$ values suggest a deeper origin for CH_4 compared to the hydrothermal environment. In line with abiotic CH_4 production experiments (e.g. McCollom, 2016) and interpretations of the origin of abiotic CH_4 in seafloor hydrothermal vents, the formation of a superheated vapor phase in some geothermal systems could provide a favorable environment for abiotic CH_4 production.

Abiotic synthesis of hydrocarbons through the serpentinization of mantle rocks in marine hydrothermal environments is supported by a growing body of evidence (Proskurowski et al., 2008; Lang et al., 2010; Ménez et al., 2018; Wang et al., 2018; Klein et al., 2019). As mentioned above, the reducing conditions prevailing in these environments may be more conducive to CH_4 production compared to the more oxidizing conditions of subaerial geothermal systems. However, the mechanism may be similar in many regards, following reaction 1 and controlled by fH_2 which is determined by fluid-rock reaction progress and mineral assemblages (Stefánsson, 2017; Leong and Shock, 2020), possibly aided by the presence of a vapor phase (McCollom, 2016). The measured CH_4/CO_2 ratios in marine systems tend to be higher than those of geothermal systems, which could reflect this difference in redox conditions. Moreover, the apparent clumped temperatures reported here are higher than those reported for marine systems (Fig. 8A), which could either reflect the higher kinetic barriers to overcome in more oxidizing systems, or longer residence times and thus lower temperature equilibration of magmatic fluids in the oceanic crust (or both).

Conclusions

Methane isotopologue distributions in steam vents and geothermal well fluids from Iceland and Nisyros are characterized by relatively low $\Delta^{13}CH_3D$ values (0.82 to 1.77‰), reflecting the generation of methane and subsequent equilibration at high temperatures generally in excess of 300°C. The lowest $\Delta^{13}CH_3D$ values were measured at exploited geothermal wells in Krafla and Námafjall in Iceland. These low $\Delta^{13}CH_3D$ values are associated with low δD_{CH4} and $\delta^{13}C_{CH4}$ values, suggesting kinetic as opposed to equilibrium signals. These kinetic signals are consistent with methane generation by thermal cracking of organic matter, although abiotic generation of methane in superheated vapor at temperatures in excess of 400°C cannot be excluded. Partial re-equilibration of δD_{CH4} values with δD_{H2O} occurs and is best recorded in high-enthalpy fluids that may have experienced supercritical conditions for longer times. In contrast, methane samples from natural steam vent fields, including the Kerlingarfjöll in Iceland and the volcanic caldera on Nisyros island, yielded higher $\Delta^{13}CH_3D$ values from 1.10 to 1.77‰. The average of $\Delta^{13}CH_3D$ values from Nisyros island (1.32±0.21‰), with corresponding apparent equilibrium temperature of 355^{+50}_{-41}°C, are consistent with the measured reservoir temperatures of 350°C, suggesting isotopologue equilibration. From available experimental data, we estimated that isotopologue equilibration for $\Delta^{13}CH_3D$ and δD between methane and water is achieved in tens of years at 350°C. Such timescale is consistent with the observed kinetic and equilibrium signals in exploited geothermal wells and matured natural geothermal systems. It is unclear whether any $^{13}CO_2$–$^{13}CH_4$ exchange is occurring, since differences in the thermal maturity of degrading organic matter may also produce $\delta^{13}C_{CH4}$ signatures overlapping those expected for isotopic equilibrium (Fig. 2), and since calculations suggest extremely slow rates for such exchange (Fig. 7D and 8C). More experimental work simulating the conditions of geothermal environments will be required to better characterize the possible reaction mechanisms of CO_2 reduction to CH_4 and evaluate the potential for abiotic methanogenesis.

Acknowledgements

We wish to thank David Wang and Yenny Gonzalez for their assistance with methane purification and analysis. Ríkey Kjartansdóttir, Jóhann Gunnarsson-Robin, Árný E. Sveinbjörnsdóttir and Rósa Ólafsdóttir are acknowledged for their help in the field and with chemical and isotope analysis. Andrea Ricci is also thanked for feedback on results and help in the field. P.B. gratefully acknowledges financial support from an NSERC PGS-D fellowship and a Sven Treitel fellowship. This project also benefited from financial support from the NASA Astrobiology Institute "Rock Powered Life" project under cooperative agreement NNA15BB02A, from the Alfred P. Sloan Foundation via the Deep Carbon Observatory, from the Icelandic Centre for Research, grant number #152680-05, and from DFG grants FI-948-8/1 (Iceland) and FI-948-9/1 (Nisyros). We thank Jabrane Labidi and one anonymous reviewer for constructive comments that helped significantly improve the manuscript.

References

Ármannsson H. (2016) The fluid geochemistry of Icelandic high temperature geothermal areas. *Appl. Geochemistry* **66**, 14–64.

Ármannsson Halldór, Gudmundsson A., Steingrímsson B., Ármannsson H, Gudmundsson A. and Steingrimsson B. (1987) Exploration and development of the Krafla geothermal area. *Jökull*, 13–30.

Arnórsson S. (1995) Geothermal systems in Iceland: Structure and conceptual models-I. High-temperature areas. *Geothermics* **24**, 561–602.

Arnórsson S., Bjarnason J. Ö., Giroud N., Gunnarsson I. and Stefánsson A. (2006) Sampling and analysis of geothermal fluids. *Geofluids* **6**, 203–216.

Arnórsson S., Fridriksson T. and Gunnarsson I. (1998) Gas chemistry of the Krafla geothermal field, Iceland. In *Intl Symp Water-Rock Interaction, Auckland, New Zealand* p. 616.

Arnórsson S. and Gunnlaugsson E. (1985) New gas geothermometers for geothermal exploration—Calibration and application. *Geochim. Cosmochim. Acta* **49**, 1307–1325.

Arnórsson S., Gunnlaugsson E. and Svavarsson H. (1983a) The chemistry of geothermal waters in Iceland. II. Mineral equilibria and independent variables controlling water compositions. *Geochim. Cosmochim. Acta* **47**, 547–566.

Arnórsson S., Gunnlaugsson E. and Svavarsson H. (1983b) The chemistry of geothermal waters in Iceland. III. Chemical geothermometry in geothermal investigations. *Geochim. Cosmochim. Acta* **47**, 567–577.

Arnórsson S., Stefánsson A. and Bjarnason J. Ö. (2007) Fluid-fluid interactions in geothermal systems. *Rev. Mineral. Geochemistry* **65**, 259–312.

Bachmann O., Deering C. D., Ruprecht J. S., Huber C., Skopelitis A. and Schnyder C. (2012) Evolution of silicic magmas in the Kos-Nisyros volcanic center, Greece: A petrological cycle associated with caldera collapse. *Contrib. to Mineral. Petrol.* **163**, 151–166.

Bali E., Aradi L. E., Zierenberg R., Diamond L. W., Pettke T., Szabó Á., Guðfinnsson G. H., Friðleifsson G. Ó. and Szabó C. (2020) Geothermal energy and ore-forming potential of 600 °C mid-ocean-ridge hydrothermal fluids. *Geology* **48**, 1221–1225.

Balk M., Bose M., Ertem G., Rogoff D. A., Rothschild L. J. and Freund F. T. (2009) Oxidation of water to hydrogen peroxide at the rock-water interface due to stress-activated electric currents in rocks. *Earth Planet. Sci. Lett.* **283**, 87–92.

Bardo R. D. and Wolfsberg M. (1976) A theoretical calculation of the equilibrium constant for the isotopic exchange reaction between H2O and HD. *J. Phys. Chem.* **80**, 1068–1071.

Berndt M. E., Allen D. E. and Seyfried W. E. (1996) Reduction of CO2 during serpentinization of olivine at 300 degrees C and 500 bar. *Geology* **24**, 351–354.

Berner U., Faber E., Scheeder G. and Panten D. (1995) Primary cracking of algal and landplant kerogens: Kinetic models of isotope variations in methane, ethane and propane. *Chem. Geol.* **126**, 233–245.

Bini G., Chiodini G., Cardellini C., Vougioukalakis G. E. and Bachmann O. (2019) Diffuse emission of CO2 and convective heat release at Nisyros caldera (Greece). *J. Volcanol. Geotherm. Res.* **376**, 44–53.

Blake P. G. and Jackson G. E. (1969) High-and low-temperature mechanisms in the thermal decomposition of acetic acid. *J. Chem. Soc. B Phys. Org.*, 94–96.

Brombach T., Caliro S., Chiodini G., Fiebig J., Hunziker J. C. and Raco B. (2003) Geochemical evidence for mixing of magmatic fluids with seawater, Nisyros hydrothermal system, Greece. *Bull. Volcanol.* **65**, 505–516.

Caliro S., Chiodini G., Galluzzo D., Granieri D., La Rocca M., Saccorotti G. and Ventura G. (2005) Recent activity of Nisyros volcano (Greece) inferred from structural, geochemical and seismological data. *Bull. Volcanol.* **67**, 358–369.

Cerrai E., Marchetti C., Renzoni R., Roseo L., Silvestri M. and Villani S. (1954) A thermal method for concentrating heavy water. Nuclear engineering, Part I. In *Chem. Eng. Progr. Symposium Ser.* Laboratori CISE, Milan, Italy.

Chiodini G., Cioni R., Leonis C., Marini L. and Raco B. (1993) Fluid geochemistry of Nisyros island, Dodecanese, Greece. *J. Volcanol. Geotherm. Res.* **56**, 95–112.

Chiodini G. and Marini L. (1998) Hydrothermal gas equilibria: The H2O-H2-CO2-CO-CH4 system. *Geochim. Cosmochim. Acta* **62**, 2673–2687.

Cioni R. and Corazza E. (1981) Medium-temperature fumarolic gas sampling. *Bull. Volcanol.* **44**, 23–29.

Cole D. R. and Chakraborty S. (2001) Rates and Mechanisms of Isotopic Exchange. *Rev. Mineral. Geochemistry* **43**, 83–223.

Craig H. (1953) The geochemistry of the stable carbon isotopes. *Geochim. Cosmochim. Acta* **3**, 53–92.

D'Amore F. and Panichi C. (1980) Evaluation of deep temperatures of hydrothermal systems by a new gas geothermometer. *Geochim. Cosmochim. Acta* **44**, 549–556.

Dias R. F., Freeman K. H., Lewan M. D. and Franks S. G. (2002) δ13C of low-molecular-weight organic acids generated by the hydrous pyrolysis of oil-prone source rocks. *Geochim. Cosmochim. Acta* **66**, 2755–2769.

Douglas P. M. J., Stolper D. A., Eiler J. M., Sessions A. L., Lawson M., Shuai Y., Bishop A., Podlaha O. G., Ferreira A. A., Santos Neto E. V., Niemann M., Steen A. S., Huang L., Chimiak L., Valentine D. L., Fiebig J., Luhmann A. J., Seyfried W. E., Etiope G., Schoell M., Inskeep W. P., Moran J. J. and Kitchen N. (2017) Methane clumped isotopes: Progress and potential for a new isotopic tracer. *Org. Geochem.* **113**, 262–282.

Duan X. and Page M. (1995) Theoretical investigation of competing mechanisms in the thermal unimolecular decomposition of acetic acid and the hydration reaction of ketene. *J. Am. Chem. Soc.* **117**, 5114–5119.

Elders W. A., Frioleifsson G. O. and Pálsson B. (2014) Iceland deep drilling project: The first well, IDDP-1, drilled into magma. *Geothermics* **49**, 1.

Eldridge D. L., Korol R., Lloyd M. K., Turner A. C., Webb M. A., Miller T. F. and Stolper D. A. (2019) Comparison of Experimental vs Theoretical Abundances of 13CH3D and 12CH2D2 for Isotopically Equilibrated Systems from 1 to 500 °C. *ACS Earth Sp. Chem.* **3**, 2747–2764.

Etiope G., Oehler D. Z. and Allen C. C. (2011) Methane emissions from Earth's degassing: Implications for Mars. *Planet. Space Sci.* **59**, 182–195.

Etiope G. and Sherwood Lollar B. (2013) Abiotic methane on earth. *Rev. Geophys.* **51**, 276–299.

Fiebig J., Chiodini G., Caliro S., Rizzo A., Spangenberg J. and Hunziker J. C. (2004) Chemical and isotopic equilibrium between CO2 and CH4 in fumarolic gas discharges: Generation of CH4 in arc magmatic-hydrothermal systems. *Geochim. Cosmochim. Acta* **68**, 2321–2334.

Fiebig J., Stefánsson A., Ricci A., Tassi F., Viveiros F., Silva C., Lopez T. M., Schreiber C., Hofmann S. and Mountain B. W. (2019) Abiogenesis not required to explain the origin of volcanic-hydrothermal hydrocarbons. *Geochemical Perspect. Lett.* **11**, 23–27.

Fiebig J., Tassi F., D'Alessandro W., Vaselli O. and Woodland A. B. (2013) Carbon-bearing gas geothermometers for volcanic-hydrothermal systems. *Chem. Geol.* **351**, 66–75.

Fiebig J., Woodland A. B., Spangenberg J. and Oschmann W. (2007) Natural evidence for rapid abiogenic hydrothermal generation of CH4. *Geochim. Cosmochim. Acta* **71**, 3028–3039.

Fournier R. O. (1999) Hydrothermal processes related to movement of fluid from plastic into brittle rock in the magmatic-epithermal environment. *Econ. Geol.* **94**, 1193–1211.

Fu Q., Sherwood Lollar B., Horita J., Lacrampe-Couloume G. and Seyfried W. E. (2007) Abiotic formation of hydrocarbons under hydrothermal conditions: Constraints from chemical and isotope data. *Geochim. Cosmochim. Acta* **71**, 1982–1998.

Giggenbach W. F. (1982) Carbon-13 exchange between CO2 and CH4 under geothermal conditions. *Geochim. Cosmochim. Acta* **46**, 159–165.

Giggenbach W. F. (1980) Geothermal gas equilibria. *Geochim. Cosmochim. Acta* **44**, 2021–2032.

Giggenbach W. F. (1988) Geothermal solute equilibria. Derivation of Na-K-Mg-Ca geoindicators. *Geochim. Cosmochim. Acta* **52**, 2749–2765.

Giggenbach W. F. (1987) Redox processes governing the chemistry of fumarolic gas discharges from White Island, New Zealand. *Appl. Geochemistry* **2**, 143–161.

Giggenbach W. F. (1997) Relative importance of thermodynamic and kinetic processes in governing the chemical and isotopic composition of carbon gases in high-heat flow sedimentary basins. *Geochim. Cosmochim. Acta* **61**, 3763–3785.

Giunta T., Labidi J., Kohl I. E., Ruffine L., Donval J. P., Géli L., Çağatay M. N., Lu H. and Young E. D. (2021) Evidence for methane isotopic bond re-ordering in gas reservoirs sourcing cold seeps from the Sea of Marmara. *Earth Planet. Sci. Lett.* **553**.

Gonzalez Y., Nelson D. D., Shorter J. H., McManus J. B., Dyroff C., Formolo M., Wang D. T., Western C. M. and Ono S. (2019) Precise Measurements of 12CH2D2 by Tunable Infrared Laser Direct Absorption Spectroscopy. *Anal. Chem.* **91**, 14967–14974.

Gudmundsson A. (2000) Dynamics of volcanic systems in Iceland: Example of tectonism and volcanism at Juxtaposed hot spot and mid-ocean ridge systems. *Annu. Rev. Earth Planet. Sci.* **28**, 107–140.

Gunnarsson I. and Arnórsson S. (2000) Amorphous silica solubility and the thermodynamic properties of H4SiO4° in the range of 0°to 350°C at P(sat). *Geochim. Cosmochim. Acta* **64**, 2295–2307.

Hayba D. O. and Ingebritsen S. E. (1997) Multiphase groundwater flow near cooling plutons. *J. Geophys. Res. B Solid Earth* **102**, 12235–12252.

Heřmanská M., Stefánsson A. and Scott S. (2019) Supercritical fluids around magmatic intrusions: IDDP-1 at Krafla, Iceland. *Geothermics* **78**, 101–110.

Horibe Y. and Craig H. (1995) D H fractionation in the system methane-hydrogen-water. *Geochim. Cosmochim. Acta* **59**, 5209–5217.

Horita J. (2001) Carbon isotope exchange in the system CO2-CH4 at elevated temperatures. *Geochim. Cosmochim. Acta* **65**, 1907–1919.

Horita J. (1988) Hydrogen isotope analysis of natural waters using an H2-water equilibration method: A special implication to brines. *Chem. Geol. Isot. Geosci. Sect.* **72**, 89–94.

Horita J. and Wesolowski D. J. (1994) Liquid-vapor fractionation of oxygen and hydrogen isotopes of water from the freezing to the critical temperature. *Geochim. Cosmochim. Acta* **58**, 3425–2437.

Huff G. A. and Satterfield C. N. (1984) Intrinsic kinetics of the Fischer-Tropsch synthesis on a Reduced Fused-Magnetite Catalyst. *Ind. Eng. Chem. Process Des. Dev.* **23**, 696–705.

Hulston J. R. and McCabe W. J. (1962) Mass spectrometer measurements in the thermal areas of New Zealand. Part 2. Carbon isotopic ratios. *Geochim. Cosmochim. Acta* **26**, 399–410.

Hunt J. M. (1996) Petroleum geology and geochemistry. *emanandCompanyt SanFrancisco, 197g. 26i* **273**.

Hut G. (1987) Consultants' group meeting on stable isotope reference samples for geochemical and hydrological investigations. *Int. At. Energy Agency*, 49.

Johnson J. W., Oelkers E. H. and Helgeson H. C. (1992) *SUPCRT92: A software package for calculating the standard molal thermodynamic properties of minerals, gases, aqueous species, and reactions from 1 to 5000 bar and 0 to 1000°C.*,

Kadko D., Gronvold K. and Butterfield D. (2007) Application of radium isotopes to determine crustal residence times of hydrothermal fluids from two sites on the Reykjanes Peninsula, Iceland. *Geochim. Cosmochim. Acta* **71**, 6019–6029.

Kasting J. F., Pavlov A. A. and Siefert J. L. (2001) A coupled ecosystem-climate model for predicting the methane concentration in the archean atmosphere. *Orig. Life Evol. Biosph.* **31**, 271–285.

Kavouridis T., Kuris D., Leonis C., Liberopoulou V., Leontiadis J., Panichi C., La Ruffa G. and Caprai A. (1999) Isotope and chemical studies for a geothermal assessment of the island of Nisyros (Greece). *Geothermics* **28**, 219–239.

Kelley D. S. (1996) Methane-rich fluids in the oceanic crust. *J. Geophys. Res. B Solid Earth* **101**, 2943–2962.

Kita I., Matsuo S. and Wakita H. (1982) H2 generation by reaction between H2O and crushed rock: an experimental study on H2 degassing from the active fault zone. *J. Geophys. Res.* **87**, 789–795.

Klein F., Grozeva N. G. and Seewald J. S. (2019) Abiotic methane synthesis and serpentinization in olivine-hosted fluid inclusions. *Proc. Natl. Acad. Sci.* **116**, 17666–17672.

Koepp M. (1978) D/H isotope exchange reaction between petroleum and water: A contributory determinant for D/H-isotope ratios in crude oil? In *Short Papers of the Fourth International Conference. Geochronology. Cosmochronology. Isotope Geology, 1978* US Geological Survey. pp. 221–222.

Labidi J., Young E. D., Giunta T., Kohl I. E., Seewald J., Tang H., Lilley M. D. and Früh-Green G. L. (2020) Methane thermometry in deep-sea hydrothermal systems: Evidence for re-ordering of doubly-substituted isotopologues during fluid cooling. *Geochim. Cosmochim. Acta* **288**, 248–261.

Lang S. Q., Butterfield D. A., Schulte M., Kelley D. S. and Lilley M. D. (2010) Elevated concentrations of formate, acetate and dissolved organic carbon found at the Lost City hydrothermal field. *Geochim. Cosmochim. Acta* **74**, 941–952.

Leong J. A. M. and Shock E. L. (2020) Thermodynamic constraints on the geochemistry of low-temperature, continental, serpentinization-generated fluids. *Am. J. Sci.* **320**, 185–235.

Littke R., Krooss B., Idiz E. and Frielingsdorf J. (1995) Molecular nitrogen in natural gas accumulations: generation from sedimentary organic matter at high temperatures. *Am. Assoc. Pet. Geol. Bull.* **79**, 410–430.

Liu Q. and Liu Y. (2016) Clumped-isotope signatures at equilibrium of CH4, NH3, H2O, H2S and SO2. *Geochim. Cosmochim. Acta* **175**, 252–270.

Lollar B. S., Lacrampe-Couloume G., Slater G. F., Ward J., Moser D. P., Gihring T. M., Lin L. H. and Onstott T. C. (2006) Unravelling abiogenic and biogenic sources of methane in the Earth's deep subsurface. *Chem. Geol.* **226**, 328–339.

Mackie J. C. and Doolan K. R. (1984) High-temperature kinetics of thermal decomposition of acetic acid and its products. *Int. J. Chem. Kinet.* **16**, 525–541.
Des Marais D. J., Donchin J. H., Nehring N. L. and Truesdell A. H. (1981) Molecular carbon isotopic evidence for the origin of geothermal hydrocarbons. *Nature* **292**, 826–828.
Marini L., Principe C., Chiodini G., Cioni R., Fytikas M. and Marinelli G. (1993) Hydrothermal eruptions of Nisyros (Dodecanese, Greece). Past events and present hazard. *J. Volcanol. Geotherm. Res.* **56**, 71–94.
McCollom T. M. (2016) Abiotic methane formation during experimental serpentinization of olivine. *Proc. Natl. Acad. Sci.* **113**, 13965–13970.
McCollom T. M. (2013) Laboratory simulations of abiotic hydrocarbon formation in earth's deep subsurface. *Rev. Mineral. Geochemistry* **75**, 467–494.
McCollom T. M., Lollar B. S., Lacrampe-Couloume G. and Seewald J. S. (2010) The influence of carbon source on abiotic organic synthesis and carbon isotope fractionation under hydrothermal conditions. *Geochim. Cosmochim. Acta* **74**, 2717–2740.
McCollom T. M. and Seewald J. S. (2006) Carbon isotope composition of organic compounds produced by abiotic synthesis under hydrothermal conditions. *Earth Planet. Sci. Lett.* **243**, 74–84.
McDermott J. M., Seewald J. S., German C. R. and Sylva S. P. (2015) Pathways for abiotic organic synthesis at submarine hydrothermal fields. *Proc. Natl. Acad. Sci.* **112**, 7668–7672.
Ménez B., Pisapia C., Andreani M., Jamme F., Vanbellingen Q. P., Brunelle A., Richard L., Dumas P. and Réfrégiers M. (2018) Abiotic synthesis of amino acids in the recesses of the oceanic lithosphere. *Nature* **564**, 59–63.
Ohmoto H. and Lasaga A. C. (1982) Kinetics of reactions between aqueous sulfates and sulfides in hydrothermal systems. *Geochim. Cosmochim. Acta* **46**, 1727–1745.
Ono S., Wang D. T., Gruen D. S., Sherwood Lollar B., Zahniser M. S., McManus B. J. and Nelson D. D. (2014) Measurement of a doubly substituted methane isotopologue, 13CH3D, by tunable infrared laser direct absorption spectroscopy. *Anal. Chem.* **86**, 6487–6494.
Di Paola G. M. (1974) Volcanology and petrology of Nisyros Island (Dodecanese, Greece). *Bull. Volcanol.* **38**, 944–987.
Pester N. J., Conrad M. E., Knauss K. G. and DePaolo D. J. (2018) Kinetics of D/H isotope fractionation between molecular hydrogen and water. *Geochim. Cosmochim. Acta* **242**, 191–212.
Pope E. C., Bird D. K., Arnórsson S. and Giroud N. (2016) Hydrogeology of the Krafla geothermal system, northeast Iceland. *Geofluids* **16**, 175–197.
Proskurowski G., Lilley M. D., Seewald J. S., Früh-Green G. L., Olson E. J., Lupton J. E., Sylva S. P. and Kelley D. S. (2008) Abiogenic hydrocarbon production at Lost City hydrothermal field. *Science* **319**, 604–607.
Quigley T. M. and Mackenzie A. S. (1988) The temperatures of oil and gas formation in the sub-surface. *Nature* **333**, 549–552.
Reeves E. P. and Fiebig J. (2020) Abiotic Synthesis of Methane and Organic Compounds in Earth's Lithosphere. *Elements* **16**, 25–31.
Reeves E. P., Seewald J. S. and Sylva S. P. (2012) Hydrogen isotope exchange between n-alkanes and water under hydrothermal conditions. *Geochim. Cosmochim. Acta* **77**, 582–599.
Richet P., Bottinga Y. and Javoy M. (1977) A review of hydrogen, carbon, nitrogen, oxygen, sulphur, and chlorine stable isotope fractionation among gaseous molecules. *Annu. Rev. Earth Planet. Sci.* **5**, 65–110.
Sackett W. M. (1993) Carbon isotope exchange between methane and amorphous carbon at 700°C. *Org. Geochem.* **20**, 43–45.
Scott S., Driesner T. and Weis P. (2015) Geologic controls on supercritical geothermal resources above magmatic intrusions. *Nat. Commun.* **6**, 1–6.
Scott S., Driesner T. and Weis P. (2016) The thermal structure and temporal evolution of high-enthalpy geothermal systems. *Geothermics* **62**, 33–47.
Seewald J. S., Zolotov M. Y. and McCollom T. (2006) Experimental investigation of single carbon compounds under hydrothermal conditions. *Geochim. Cosmochim. Acta* **70**, 446–460.
Sherwood Lollar B., Frape S. K., Weise S. M., Fritz P., Macko S. A. and Welhan J. A. (1993) Abiogenic methanogenesis in crystalline rocks. *Geochim. Cosmochim. Acta* **57**, 5087–5097.
Shock E. L. (1992) Chemical environments of submarine hydrothermal systems. *Orig. Life Evol. Biosph.* **22**, 67–107.
Shuai Y., Douglas P. M. J., Zhang S., Stolper D. A., Ellis G. S., Lawson M., Lewan M. D., Formolo M., Mi J., He K., Hu G. and Eiler J. M. (2018a) Equilibrium and non-equilibrium controls on the abundances of clumped

isotopologues of methane during thermogenic formation in laboratory experiments: Implications for the chemistry of pyrolysis and the origins of natural gases. *Geochim. Cosmochim. Acta* **223**, 159–174.
Shuai Y., Etiope G., Zhang S., Douglas P. M. J., Huang L. and Eiler J. M. (2018b) Methane clumped isotopes in the Songliao Basin (China): New insights into abiotic vs. biotic hydrocarbon formation. *Earth Planet. Sci. Lett.* **482**, 213–221.
Smith G. P., Golden D. M., Frenklach M., Moriarty N. W., Eiteneer B., Goldenberg M., Bowman C. T., Hanson R. K., Song S., Gardiner Jr. W. C., Lissianski V. V and Qin Z. (2000) GRI-Mech 3.0. *Http://Www.Me.Berkeley.Edu/Gri_Mech/*.
Stefánsson A. (2017) Gas chemistry of Icelandic thermal fluids. *J. Volcanol. Geotherm. Res.* **346**, 81–94.
Stefánsson A., Gunnarsson I. and Giroud N. (2007) New methods for the direct determination of dissolved inorganic, organic and total carbon in natural waters by Reagent-Free™ Ion Chromatography and inductively coupled plasma atomic emission spectrometry. *Anal. Chim. Acta* **582**, 69–74.
Stefánsson A., Hilton D. R., Sveinbjörnsdóttir Á. E., Torssander P., Heinemeier J., Barnes J. D., Ono S., Halldórsson S. A., Fiebig J. and Arnórsson S. (2017) Isotope systematics of Icelandic thermal fluids. *J. Volcanol. Geotherm. Res.* **337**, 146–164.
Stefánsson A., Keller N. S., Robin J. G. and Ono S. (2015) Multiple sulfur isotope systematics of Icelandic geothermal fluids and the source and reactions of sulfur in volcanic geothermal systems at divergent plate boundaries. *Geochim. Cosmochim. Acta* **165**, 307–323.
Stolper D. A., Lawson M., Davis C. L., Ferreira A. A., Santos Neto E. V., Ellis G. S., Lewan M. D., Martini A. M., Tang Y., Schoell M., Sessions A. L. and Eiler J. M. (2014a) Formation temperatures of thermogenic and biogenic methane. *Science* **344**, 1500–1503.
Stolper D. A., Lawson M., Formolo M. J., Davis C. L., Douglas P. M. J. and Eiler J. M. (2017) The utility of methane clumped isotopes to constrain the origins of methane in natural gas accumulations. *Geol. Soc. London, Spec. Publ.* **4**, SP468.3.
Stolper D. A., Sessions A. L., Ferreira A. A., Santos Neto E. V., Schimmelmann A., Shusta S. S., Valentine D. L. and Eiler J. M. (2014b) Combined 13C-D and D-D clumping in methane: Methods and preliminary results. *Geochim. Cosmochim. Acta* **126**, 169–191.
Suess H. E. (1949) Das Gleichgewicht H2 + HDO = HD + H2O und die weiteren Austauschgleichgewichte im System H2, D2 und H2O. *Zeitschrift fur Naturforsch. A* **4**, 328–332.
Sutherland J. W., Su M. C. and Michael J. V. (2001) Rate constants for H + CH4, CH3 + H2, and CH4 dissociation at high temperature. *Int. J. Chem. Kinet.* **33**, 669–684.
Taran Y. A., Kliger G. A., Cienfuegos E. and Shuykin A. N. (2010) Carbon and hydrogen isotopic compositions of products of open-system catalytic hydrogenation of CO2: Implications for abiogenic hydrocarbons in Earth's crust. *Geochim. Cosmochim. Acta* **74**, 6112–6125.
Tissot B. P. and Welte D. H. (1978) *Petroleum Formation and Occurrence*.,
Ueno Y., Yamada K., Yoshida N., Maruyama S. and Isozaki Y. (2006) Evidence from fluid inclusions for microbial methanogenesis in the early Archaean era. *Nature* **440**, 516–519.
Wang D. T., Gruen D. S., Sherwood Lollar B., Hinrichs K. U., Stewart L. C., Holden J. F., Hristov A. N., Pohlman J. W., Morrill P. L., Könneke M., Delwiche K. B., Reeves E. P., Sutcliffe C. N., Ritter D. J., Seewald J. S., McIntosh J. C., Hemond H. F., Kubo M. D., Cardace D., Hoehler T. M. and Ono S. (2015) Nonequilibrium clumped isotope signals in microbial methane. *Science* **348**, 428–431.
Wang D. T., Reeves E. P., McDermott J. M., Seewald J. S. and Ono S. (2018) Clumped isotopologue constraints on the origin of methane at seafloor hot springs. *Geochim. Cosmochim. Acta* **223**, 141–158.
Webb M. A. and Miller T. F. (2014) Position-specific and clumped stable isotope studies: Comparison of the urey and path-integral approaches for carbon dioxide, nitrous oxide, methane, and propane. *J. Phys. Chem. A* **118**, 467–474.
Whitehill A. R., Joelsson L. M. T., Schmidt J. A., Wang D. T., Johnson M. S. and Ono S. (2017) Clumped isotope effects during OH and Cl oxidation of methane. *Geochim. Cosmochim. Acta* **196**, 307–325.
Young E. D., Kohl I. E., Lollar B. S., Etiope G., Rumble D., Li (李姝宁) S., Haghnegahdar M. A., Schauble E. A., McCain K. A., Foustoukos D. I., Sutclife C., Warr O., Ballentine C. J., Onstott T. C., Hosgormez H., Neubeck A., Marques J. M., Pérez-Rodríguez I., Rowe A. R., LaRowe D. E., Magnabosco C., Yeung L. Y., Ash J. L. and Bryndzia L. T. (2017) The relative abundances of resolvedl2CH2D2and13CH3D and mechanisms controlling isotopic bond ordering in abiotic and biotic methane gases. *Geochim. Cosmochim. Acta* **203**, 235–264.

Zimmerman W. H. and Bukur D. B. (1990) Reaction kinetics over iron catalysts used for the fischer-tropsch synthesis. *Can. J. Chem. Eng.* **68**, 292–301.

Table 1: Gas chemistry of geothermal well discharges (Iceland) and fumaroles (Iceland and Nisyros, Greece)

Sample Name	Location	H_2O	CO_2	H_2S	H_2	N_2	Ar	O_2	CH_4	CO	C_1/C_{2+}
Iceland wells											
15-AS-07	Krafla, w32	998030	1317	426	194	21.9	0.35	0.200	1.33	8.77E-03	256
15-AS-08	Krafla, w16	990059	8411	818	683	17.4	0.21	0.081	4.53	6.30E-03	248
15-AS-9	Námafjall, w13	998643	583	421	316	22.6	0.34	0.097	1.93	1.13E-02	742
15-AS-10	Námafjall, w9	997055	1107	837	896	63.0	1.05	0.256	26.9	1.26E-02	596
15-AS-17	Reykjanes, w15	994709	5069	156	11.8	48.7	0.90	0.107	1.25	3.03E-03	132
15-AS-15	Haedarendi, w7	464561	533293	140	15.7	1752.3	26.60	11.304	186	1.42E-02	2343
Iceland fumaroles											
15-AS-01*	Krysuvik	994240	5263	363	107	23.0	0.44	0.146	1.41	2.14E-03	316
15-AS-03	Kerlingarfjoll	995899	3239	406	413	37.7	0.54	0.200	2.71	1.70E-03	823
15-AS-05	Kerlingarfjoll	995991	2734	626	613	31.0	0.34	0.191	4.41	1.95E-04	870
15-AS-06	Kerlingarfjoll	996133	2693	554	592	21.8	0.25	0.103	4.59	3.54E-05	1016
15-AS-11	Námafjall	999129	635	132	20.8	60.0	1.32	1.983	20.0	*n.m.*	566
Nisyros fumaroles											
K7	Kaminakia	921217	69842	6098	871	404	5.6	7.4	1554	0.079	*n.m.*
K6	Kaminakia	946953	47480	3199	334	175	3.2	2.0	1854	0.053	*n.m.*
S4-lo	Stefanos	985744	10925	3059	109	53.3	0.78	0.90	108	0.242	*n.m.*
S4-hi	Stefanos	986871	10091	2828	90	32.0	0.45	0.29	86.8	0.079	*n.m.*
S15	Stefanos	986042	10431	3290	109	31.7	0.69	1.1	93.9	0.045	*n.m.*
A14	Phlegeton	982341	13728	3679	144	74.7	1.1	4.9	26.8	0.037	*n.m.*
A13	Phlegeton	977011	16788	3197	165	2763	40.5	4.9	30.5	0.025	*n.m.*
PP9S	Polybotes Mikros	989379	8779	1670	104	36.1	0.75	0.66	29.8	*n.m.*	*n.m.*
PP9N	Polybotes Mikros	986586	10824	2360	130	51.7	0.76	2.0	44.4	0.014	*n.m.*

All concentrations in µmol/mol. *averaged composition of 15-AS-01 and 15-AS-02. C_{2+} refer to C_2-C_6 values of alkanes and alkenes. *n.m.*: not measured

Table 2: Isotopic composition of H and C in H_2O-H_2-CO_2-CH_4 fluids

Sample Name	Location	δD_{H2O} (‰)	δD_{CH4} (‰)	$\delta^{13}C_{CH4}$ (‰)	$\delta^{13}C_{CO2}$ (‰)	$\Delta^{13}CH_3D$ (‰)	95% CI (‰)	$T_{\Delta^{13}CH_3D}$ (°C)
Iceland wells								
15-AS-07	Krafla, w32	-82.4	-319.6	-39.6	-3.8	0.82	0.34	490^{+163}_{-99}
15-AS-08	Krafla, w16	-83.1	-242.9	-38.7	-3.5	0.95	0.33	447^{+129}_{-84}
15-AS-9	Namafjall, w13	-94.8	-262.4	-37.4	-3.7	1.22	0.28	376^{+73}_{-55}
15-AS-10	Namafjall, w9	-88.5	-293.7	-35.8	-3.0	0.94	0.18	450^{+61}_{-49}
15-AS-17	Reykjanes, w15	-27.8	-165.0	-31.5	-2.8	1.21	0.15	379^{+37}_{-32}
15-AS-15	Haedarendi, w7	-86.1	-215.7	-27.0	-2.4	1.69	0.23	290^{+38}_{-32}
Iceland fumaroles								
15-AS-1**	Krysuvik	--	-205.5	-36.4	-3.2	1.55	0.22	312^{+41}_{-34}
15-AS-03*	Kerlingarfjoll†	*-82*	-201.0	-25.0	-3.2	1.31	0.44	357^{+116}_{-76}
15-AS-03 (1)			-200.8	-24.6		1.09	0.40	408^{+133}_{-85}
15-AS-03 (2)			-201.1	-25.4		1.53	0.20	316^{+36}_{-31}
15-AS-05	Kerlingarfjoll†	*-86*	-201.4	-27.2	-3.1	1.34	0.34	351^{+82}_{-60}
15-AS-06	Kerlingarfjoll†	*-88*	-201.0	-27.2	-3.0	1.32	0.14	355^{+30}_{-27}
15-AS-11	Namafjall	--	-310.9	-35.2	-3.0	1.22	0.48	376^{+145}_{-88}
Nisyros fumaroles								
K7	Kaminakia	-56.5	-125.8	-22.5	-1.5	1.16	0.21	390^{+56}_{-45}
K6	Kaminakia	-9.1	-126.6	-22.4	-1.9	1.10	0.40	405^{+133}_{-85}
S4-lo	Stefanos	-10.7	-125.1	-23.3	-1.4	1.24	0.20	372^{+48}_{-40}
S4-hi	Stefanos	-11.3	-125.0	-23.3	-1.6	1.37	0.30	345^{+69}_{-52}
S15	Stefanos	-13.8	-125.1	-23.4	-0.9	1.20	0.24	381^{+63}_{-49}
A14	Phlegeton	-4.5	-135.4	-23.4	-0.9	1.77	0.34	278^{+56}_{-44}
A13	Phlegeton	-4.8	-135.4	-23.3	-1.3	1.14	0.37	395^{+113}_{-76}
PP9S	Polybotes Mikros	-10.9	-124.4	-21.8	-0.8	1.40	0.19	339^{+39}_{-33}
PP9N	Polybotes Mikros	-10.4	-124.5	-22.0	-1.0	1.50	0.67	321^{+166}_{-93}

Measurements from Gonzalez et al. (2019)

$\Delta^{13}CH_3D$ (‰)	$T_{\Delta^{13}CH_3D}$ (°C)	$\Delta^{12}CH_2D_2$ (‰)	$T_{\Delta^{12}CH_2D_2}$ (°C)
0.97 ± 0.10	447^{+26}_{-23}	0.2 ± 0.4	860^{+112}_{-91}
1.14 ± 0.30	400^{+90}_{-65}	-0.01 ± 0.6	>769

*duplicate sample: $\delta 1^3C_{CH4}$-δD_{CH4}-$\Delta^{13}CH_3D$ values represent averages of the two measurements shown below, and 2σ values are compounded errors. **composite sample (15-AS-01+15-AS-02). †δD_{H2O} values of Kerlingarfjoll samples were not measured, but were approximated as a likely δD_{H2O} range for local meteoric water (Stefansson et al. 2017), consistent with a narrow range of δD values in Iceland's dilute hydrothermal systems (e.g. see Fig. 7A). Assigned values are italicized.

Table 3: Chemical and isotopic geothermometers discussed in this study

Reactions	Temperature dependence	Source
$SiO_{2,s} + 2H_2O \rightleftharpoons H_4SiO_4^\circ$	$\log K_{qtz} - 34.188 + 197.47 * T^{-1} - 5.851 * 10^{-6} * T^2 + 12.245 * \log T$	(a)
T_{CO2} (empirical)*	$T_{CO2} = 121.8 + 72.012Q - 11.068Q^2 + 4.724Q^3$	(b,c)
T_{H2S} (empirical)*	$T_{H2S} = 177.6 + 66.152Q + 4.811Q^2$	(b,c)
$T_{CO2/N2}$ (empirical)*	$T_{CO2/N2} = 173.2 + 48.751Q + 7.599Q^2 + 1.739Q^3$	(b,c)
$CH_4 + HDO \rightleftharpoons CH_3D + H_2O$	$\alpha_{H_2O-CH_4} = 1.0997 + 8.456 * \left(\frac{10^3}{T^2}\right) + 0.9611 * \left(\frac{10^9}{T^4}\right) - 27.82 * \left(\frac{10^{12}}{T^6}\right)$	(f)
$^{12}CH_3D + {}^{13}CH_4 \rightleftharpoons {}^{13}CH_3D + {}^{12}CH_4$	$\Delta^{13}CH_3D(T) = -0.11006\left(\frac{10^3}{T}\right)^3 + 1.04151\left(\frac{10^3}{T}\right)^2 - 0.55235\left(\frac{10^3}{T}\right)$	(g)
$^{12}CO_2 + {}^{13}CH_4 \rightleftharpoons {}^{13}CO_2 + {}^{12}CH_4$	$1000 \ln \alpha_{CO_2-CH_4} = 0.16 + 11.754 * \left(\frac{10^6}{T^2}\right) - 2.3655 * \left(\frac{10^9}{T^3}\right) + 0.2054 * \left(\frac{10^{12}}{T^4}\right)$	(d,e)

(a) Gunnarsson and Arnórsson (2000) ; (b) Arnórsson et al. (1998), updated from (c) Arnórsson and Gunnlaugsson (1985); (d) Horita (2001); (e) Richet et al. (1977); (f) Horibe and Craig (1995); Whitehill et al., (2017).*Q is the logarithm of the concentration (in mmol/kg) or of the concentration ratio.

Table 4: Temperature-depth characteristics of boreholes, and inferred temperatures from gas geothermometry for fumaroles

Sample Name	Location	Borehole depth (km)	T_{vent} (°C)	$T_{res,\ measured}$ (°C)	T_{qtz} (°C)	T_{gas} (°C)	$T_{\Delta^{13}CH_3D}$ (°C)	Discharge enthalpy (kJ/kg)
Iceland wells								
15-AS-07	Krafla, w32	1.9		250	249	273	490^{+163}_{-99}	1253
15-AS-08	Krafla, w16	2.0		270	264	339	447^{+129}_{-84}	2767
15-AS-9	Námafjall, w13	2.2		290	290	254	376^{+73}_{-55}	1544
15-AS-10	Námafjall, w9	1.3		235	236	264	450^{+61}_{-49}	1083
15-AS-17	Reykjanes, w15	2.5		290	281	287	379^{+37}_{-32}	
15-AS-15	Haedarendi, w7	0.9		170		222*	290^{+38}_{-32}	
Iceland fumaroles								
15-AS-1	Krýsuvík					309	312^{+41}_{-34}	
15-AS-03	Kerlingarfjöll					289	357^{+116}_{-76}	
15-AS-05	Kerlingarfjöll					292	351^{+82}_{-60}	
15-AS-06	Kerlingarfjöll					295	355^{+30}_{-27}	
15-AS-11	Námafjall					232	376^{+145}_{-88}	
Nisyros								
K7	Kaminakia		97			356**	390^{+56}_{-45}	
K6	Kaminakia		97			355**	405^{+133}_{-85}	
S4-lo	Stefanos		102			345	372^{+48}_{-40}	
S4-hi	Stefanos		101			349	345^{+69}_{-52}	
S15	Stefanos		100			353	381^{+63}_{-49}	
A14	Phlegeton		102			349	$278\ ^{+56}_{-44}$	
A13	Phlegeton		102			355†	$395\ ^{+113}_{-76}$	
PP9S	Polybotes Mikros		100			336	$339\ ^{+39}_{-33}$	
PP9N	Polybotes Mikros		99			341	$321\ ^{+166}_{-93}$	

T_{gas} calculated as the average of the CO_2, H_2S and CO_2/N_2 geothermomers (Arnórsson et al., 1998), with following exceptions:
*T_{gas} from H_2S thermometer only. **CO_2-only geothermometer excluded. †CO_2/N_2 geothermometer excluded

Figure 1

Click here to access/download;Figure;CH4_paper_Fig1_schematic_2

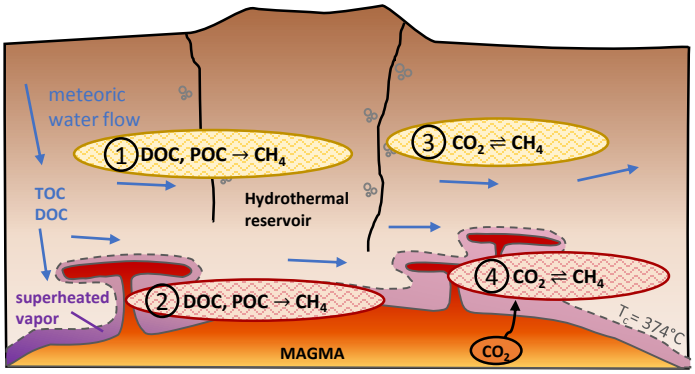

Figure 2

Click here to access/download;Figure;CH4_paper_Fig2_27may2021.pdf

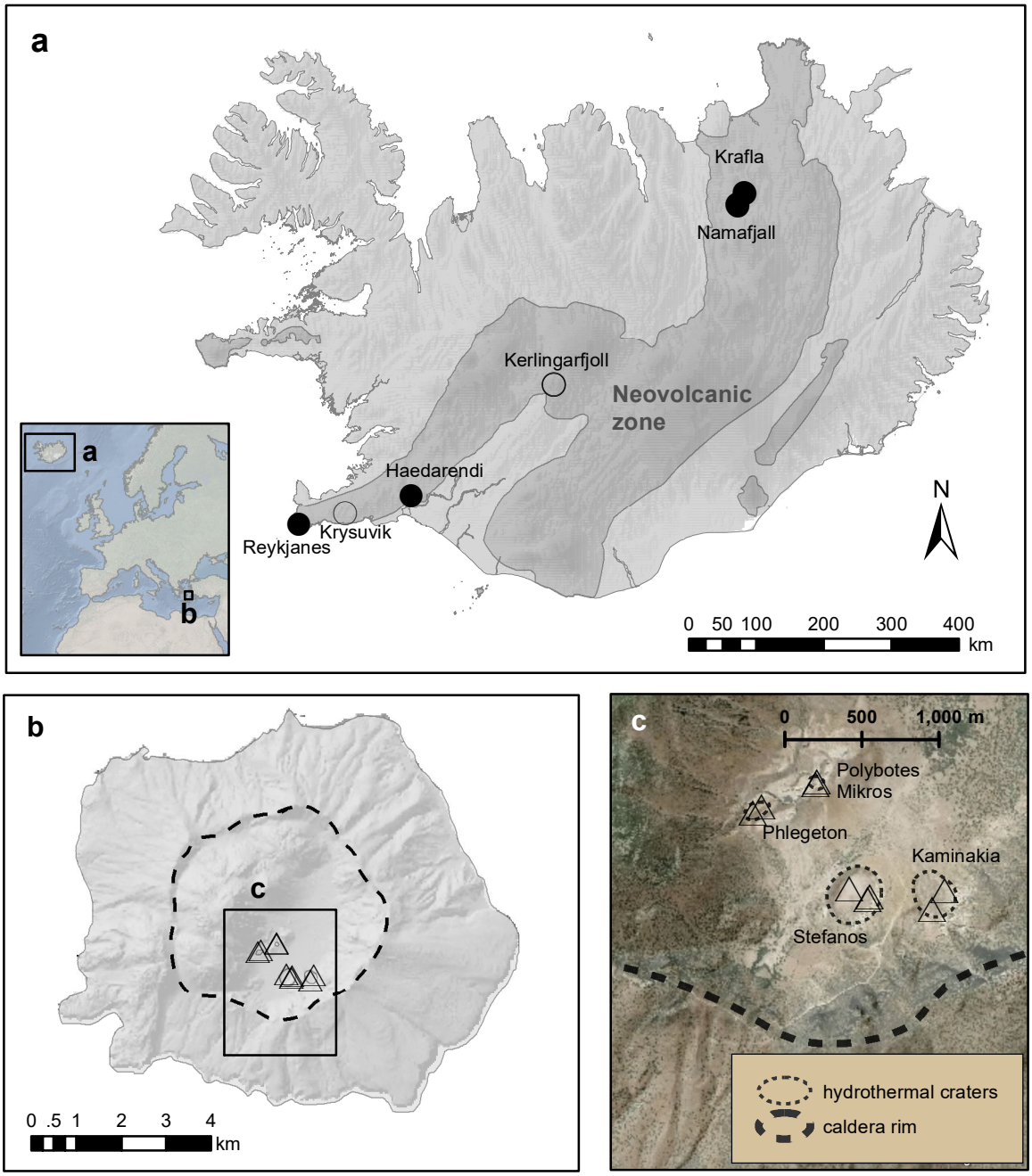

Figure 3

Click here to access/download;Figure;CH4_paper_Fig3_d13C-dD_6june2021.pdf

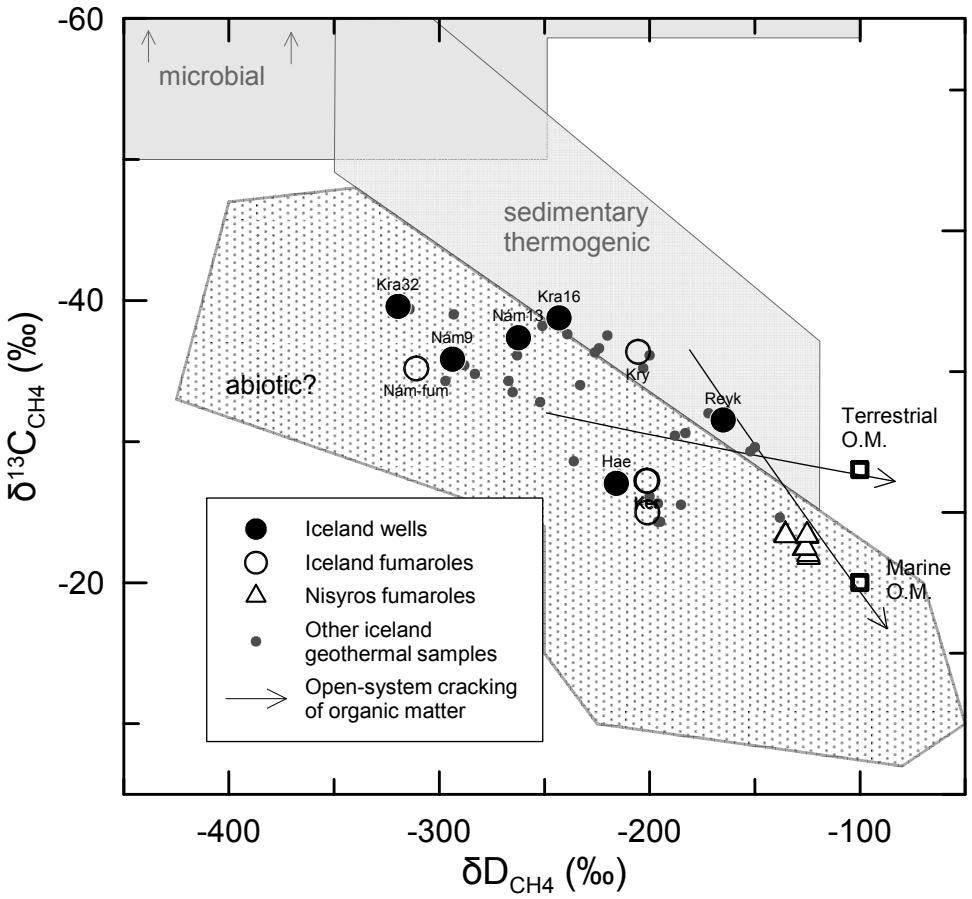

Figure 4

Click here to access/download;Figure;CH_paper_Fig4_clumped_21may2021.

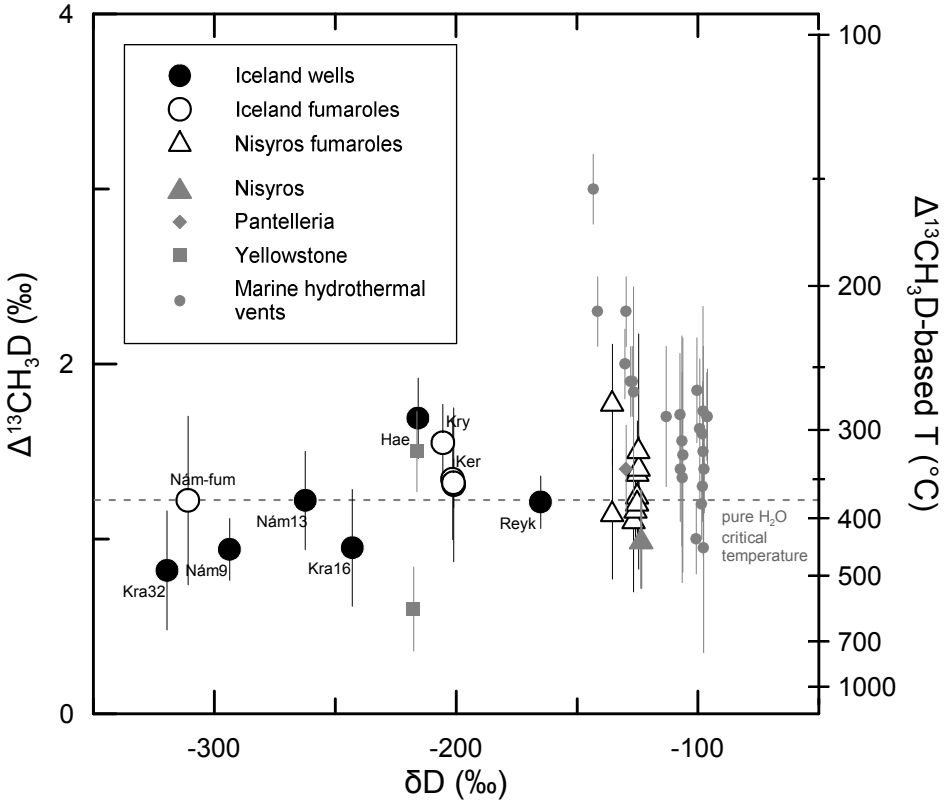

Figure 5

Click here to access/download;Figure;CH4_paper_Fig5_27may2021.pdf

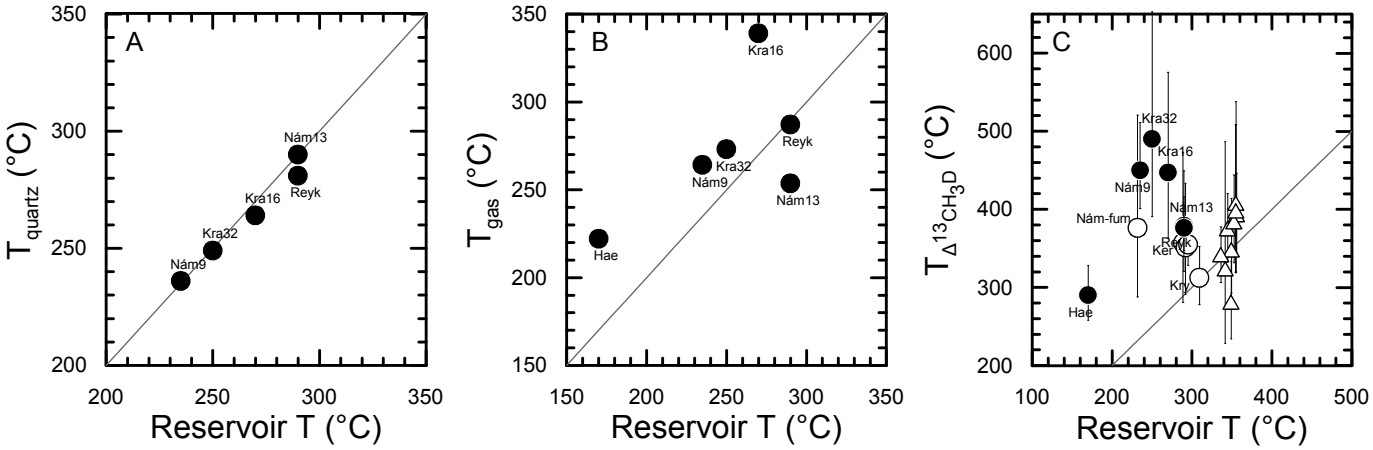

Figure 6

Click here to access/download;Figure;CH4_paper_Fig6_27may2021.pdf

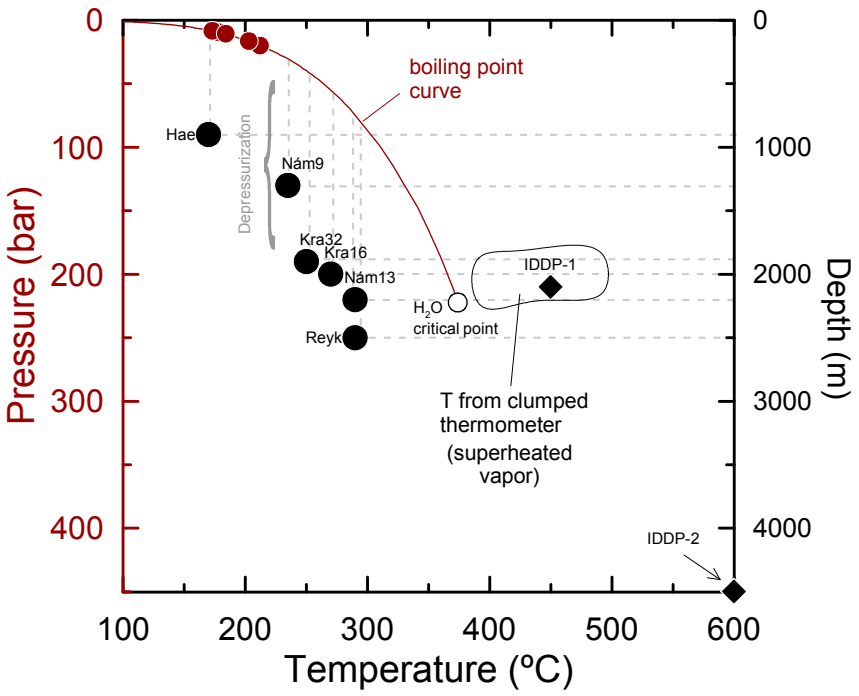

Figure 7

Click here to access/download;Figure;CH4_paper_Fig7_24may2021.pdf

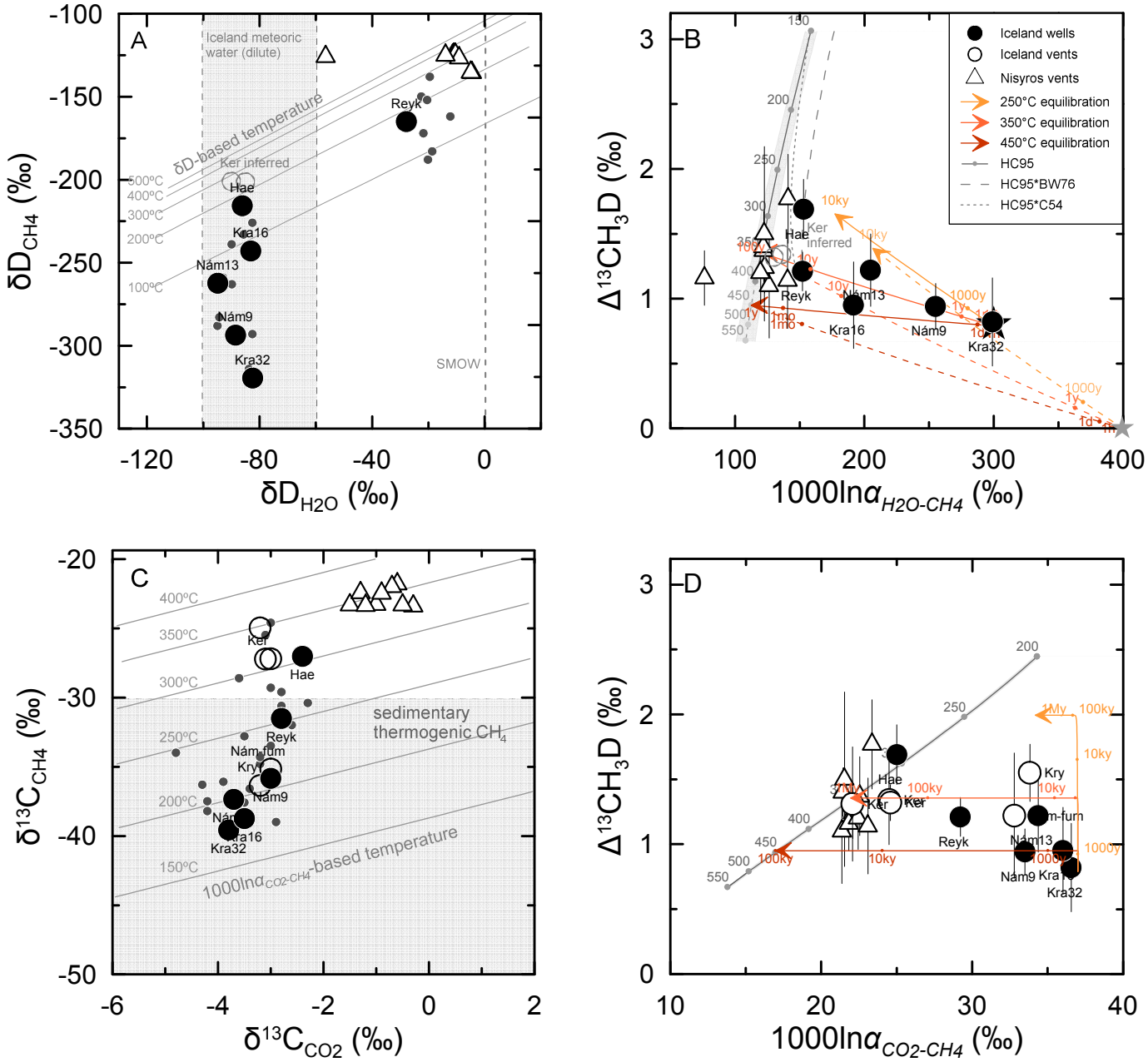

Figure 8

Click here to access/download;Figure;CH4_paper_Fig8_24may2021.pdf

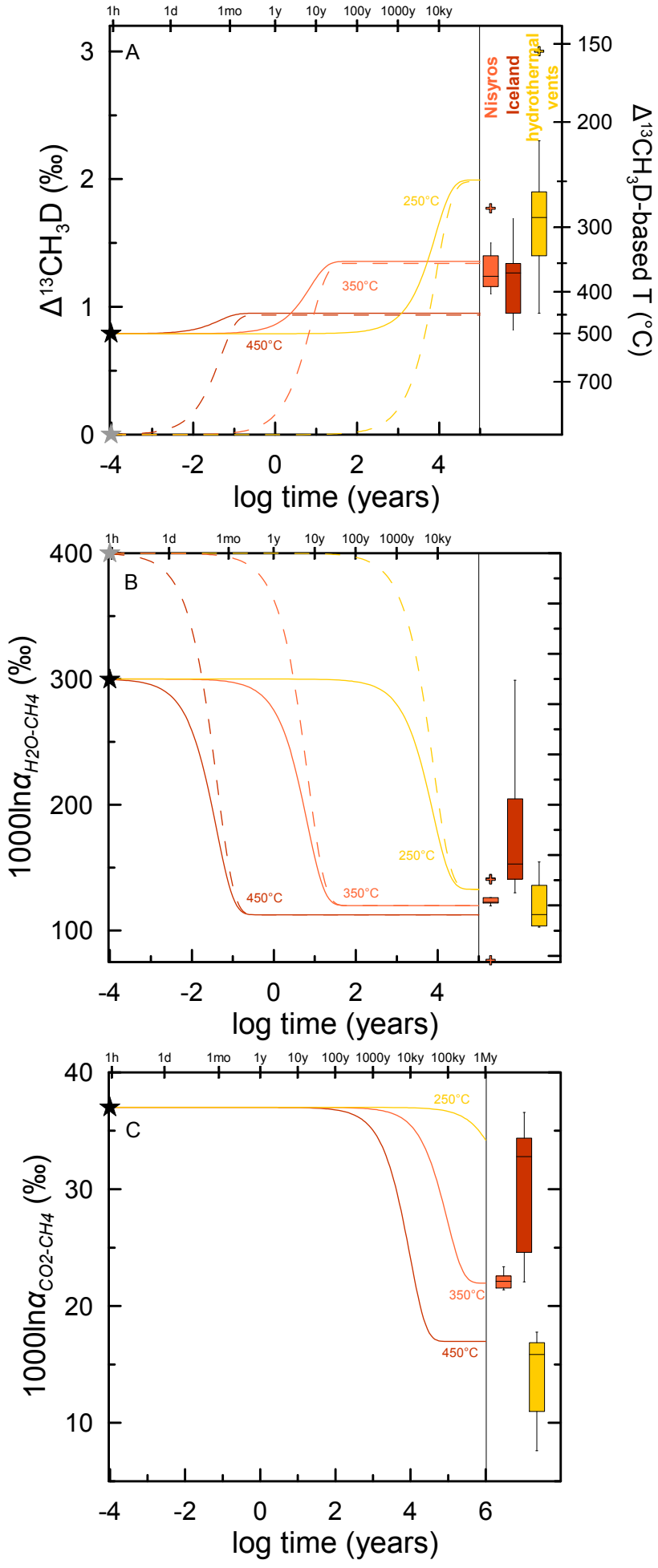

Figure 9

Click here to access/download;Figure;CH4_paper_Fig9_enthalpy_27may2021

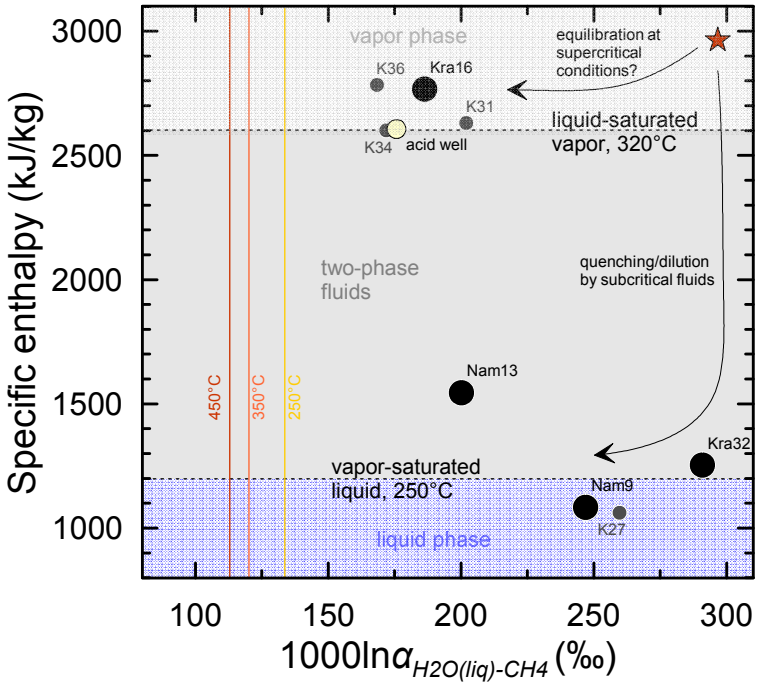

Figure 10

Click here to access/download;Figure;CH4_paper_Fig10_17june2021.pptx

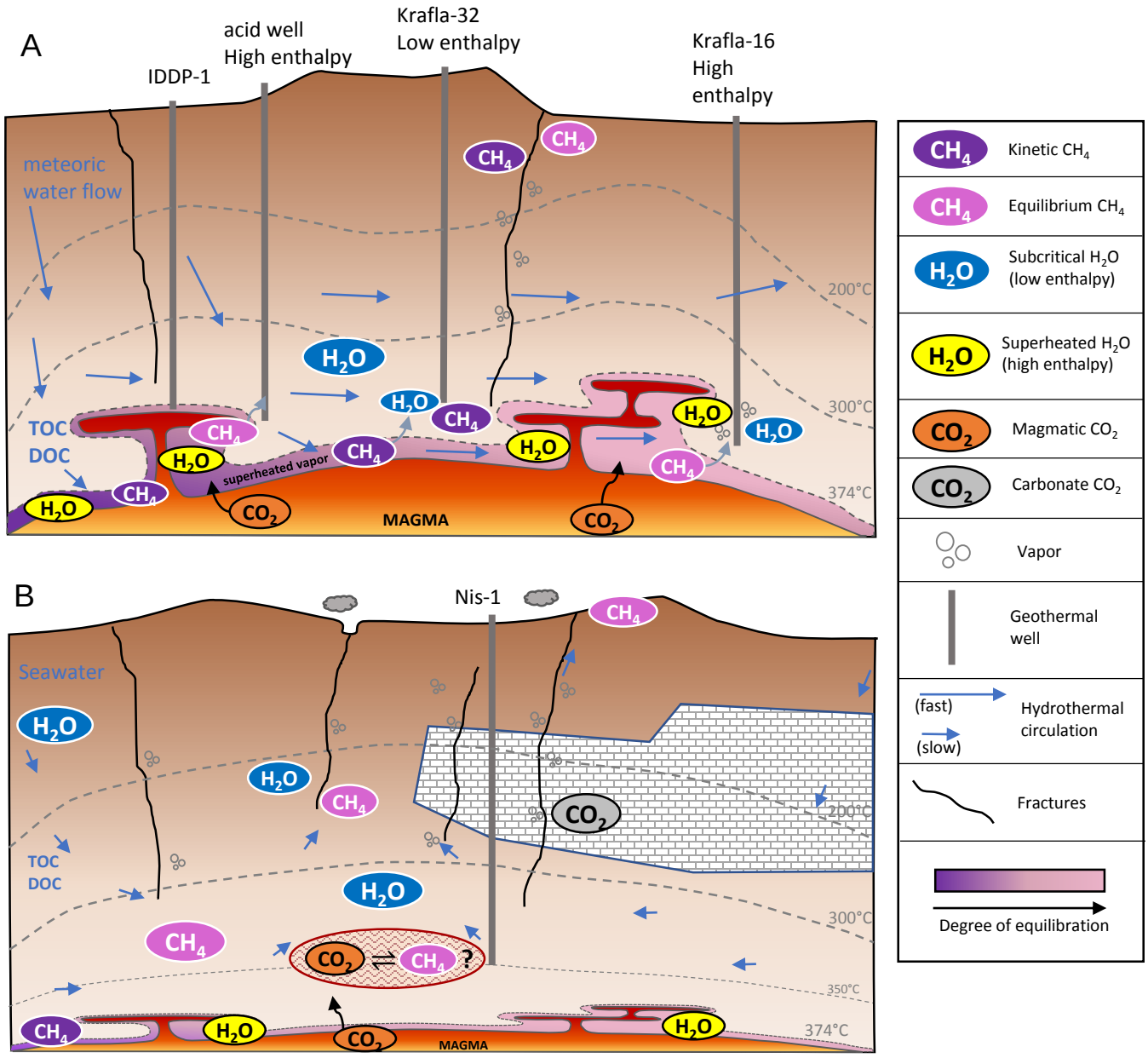

Figure captions

Figure 1: Schematic representation of a terrestrial geothermal system and possible origins for low $\Delta^{13}CH_3D$ signals observed to date. 1) methane is produced by the breakdown of organic matter (DOC, POC) contained in circulating groundwater or adsorbed on host rocks in the subcritical hydrothermal reservoir, and preserves low and kinetic $\Delta^{13}CH_3D$ signals; 2) OM is transported close to the magmatic heat source and break down to CH_4 with equilibrium $\Delta^{13}CH_3D$ signals; 3) CH_4 is produced abiotically in the subcritical reservoir via CO_2 reduction, controlled by the redox conditions of the system, preserving kinetic $\Delta^{13}CH_3D$ signals; 4) CH_4 is produced abiotically in a superheated vapor phase via reduction of magmatic CO_2 and preserves equilibrium $\Delta^{13}CH_3D$ signals.

Figure 2: Maps of Iceland (A) and Nisyros (B) showing sample locations and relevant geological features. Filled circles are geothermal well samples, and open circles and triangles are steam vents.

Figure 3: $\delta^{13}C_{CH4}$ vs δD_{CH4} values of methane analyzed in this study and Fiebig et al. (2019) [1]. Also shown are typical ranges for microbial and sedimentary thermogenic methane, and the proposed range for abiotic methane from (Etiope and Sherwood Lollar, 2013). Grey dots ("Other Iceland samples") and the modeled trends for methane produced by thermal cracking from terrestrial and marine organic matter are from Fiebig et al. (2019). These trends do not consider potential secondary exchange of CH_4 with water, which would flatten the corresponding pyrolysis slopes (Fiebig et al., 2019).

Figure 4: $\Delta^{13}CH_3D$ vs. δD_{CH4} plot showing the constancy of low $\Delta^{13}CH_3D$ values for all geothermal samples, including existing literature data from Nisyros, Pantelleria and Yellowstone (grey symbols, Douglas et al. (2017))* and from marine hydrothermal vents (Douglas et al., 2017; Wang et al., 2018 and Labidi et al., 2020). Dashed line representing the critical temperature of pure water shown for reference. *Data from Douglas et al. (2017) are Δ_{18} values (*see* text in Results section).

Figure 5: (A) Comparison of measured hydrothermal reservoir temperatures with temperatures derived by the quartz geothermometer for well samples. 1:1 line shown in grey; (B) Comparison of temperatures derived by gas geothermometry with measured reservoir temperatures for well samples. (C) Apparent equilibrium $\Delta^{13}CH_3D$-based temperatures compared with measured reservoir temperatures (wells) and calculated reservoir temperatures from gas geothermometry (vents). Symbols as in Figs. 1-3.

Figure 6: Pressure-temperature diagram showing the measured reservoir temperatures and borehole depths of sampled wells (black dots). The Pressure and Depth axes are approximately equivalent assuming hydrostatic pressure, hence samples follow the boiling point curve of water (red solid line) but plot left of the line, indicating depressurization of the hydrothermal reservoir upon intersection by wells. The sampling temperature and pressure (red circles) are along the

water vapor saturation curve. Maximum depths and temperatures of wells IDDP-1 (Krafla) and IDDP-2 (Reykjanes) also shown for reference; note that IDDP-1 stopped at 2.1 km when it encountered rhyolite magma (Elders et al., 2014).

Figure 7: Isotope and isotopologue systematics of geothermal samples, showing measured isotope values against those expected for equilibrium at different temperatures. (A) δD_{CH4} vs δD_{H2O} ; (B) $\Delta^{13}CH_3D$ vs $1000\ln\alpha_{H2O\text{-}CH4}$; (C) $\delta^{13}C_{CH4}$ vs $\delta^{13}C_{CO2}$; (D) $\Delta^{13}CH_3D$ vs $1000\ln\alpha_{CO2\text{-}CH4}$; dark grey dots in (A, C) are other Iceland samples—as in Fig. 3—reported in Fiebig et al. (2019). Colored arrows in (B, D) indicate the expected evolution of CH_4 isotopologues equilibration at different temperatures (shown in Fig. 7), starting from kinetic end-member Krafla-32 (black star). Dashed lines in Fig. 7B shows expected equilibration path from a more fractionated kinetic end-member (grey star), with $\Delta^{13}CH_3D$ = 0‰ and $1000\ln\alpha_{H2O\text{-}CH4}$ = 400‰. Equilibrium temperatures in (A) and (B) are from the calibration of Horibe and Craig (1995) (HC95); uncertainty (1σ) shown as grey envelope in (B). Dashed lines are shown when $\alpha_{H2O(l)\text{-}H2}$ factors of Bardo and Wolfsberg (1976) (HC95*BW76) and Cerrai (1954) (HC95*C54) are used with $\alpha_{CH4\text{-}H2}$ calibration of Horibe and Craig (1995). Equilibrium temperatures in (C) and (D) are from Horita (2001). Note the slower rates required for ^{13}C equilibration (D).

Figure 8: Evolution of CH_4 isotopologue signatures (A), deuterium fractionation (B) and ^{13}C fractionation (C) at various temperatures, assuming the starting CH_4 (black star) has the composition of kinetic end-member Krafla-32, or a more fractionated kinetic end-member (grey star and dashed lines) as in Fig. 7. Equilibration paths are compared to the ranges of measured values in Nisyros, Iceland and marine hydrothermal vents (box and whiskers plots).

Figure 9: Fluid enthalpy in Krafla and Námafjall well samples vs. $1000\ln\alpha_{H2O\text{-}CH4}$, showing that wells with high discharge enthalpy (Kra16, K31, K34, and K36) are closer to deuterium isotope equilibrium between H_2O and CH_4, shown for different temperatures as vertical colored lines. Black circles: samples measured in this study. $1000\ln\alpha_{H2O\text{-}CH4}$ values of grey dots and yellow circle calculated with data from Fiebig et al. (2019). Acid well (yellow circle) shown for reference, as such wells are thought to be composed of condensed superheated vapor (Heřmanská et al., 2019). Specific enthalpy values are shown as horizontal dashed lines for liquid-saturated vapor at 320°C, based on fluid ascent paths for Krafla from Scott et al. (2015), and for vapor-saturated (boiling) liquid at 250°C, corresponding to the lower bound of measured reservoir temperatures.

Figure 10: Schematic diagrams illustrating the possible sources of CH_4 and processes of generation and equilibration. An idealized representation of the Krafla geothermal system is depicted in (A), where fast fluid circulation favors the preservation of kinetic isotopologue signals. The direction of fluid circulation (e.g. Pope et al. 2016) is consistent with longer equilibration timescales for CH_4 emanating from the area surrounding well 16. An idealized representation of the Nisyros is shown in (B), where fluid circulation is slower and thus equilibration timescales are longer. All CH_4 that reaches the surface has equilibrium isotopologue distributions. (A) and (B) can be viewed as early and late stages in the evolution of geothermal systems, respectively (e.g. Scott et al., 2016).